DELFT UNIVERSITY OF TECHNOLOGY

THESIS
AESM2006

An experimental investigation of the effects of corrosion inhibitor on the mechanical properties of reservoir rock

---

Author:
Jon-Danilo Kortram (4099990)

September 30, 2020

An experimental investigation of the effects of corrosion inhibitor on the mechanical properties of reservoir rock

by

Jon-Danilo Kortram

to obtain the degree of Master of Science
at the Delft University of Technology,
to be defended publicly on Wednesday September 30, 2020 at 9:00 AM.

Student number:	4099990
Thesis committee:	Dr. A. Pluymakers
	Dr. A. Barnhoorn,
	Prof. D. Bruhn,

Abstract

Geothermal energy is one of the more sustainable alternatives to fossil fuels that could facilitate the energy transition. The production of geothermal energy incorporates the use of corrosion inhibitors to protect the steel well-parts from the corrosive production fluid. The injection of inhibitors leads to a risk of exposing the reservoir rock to these solutions. Up until now no data has been published to describe the effects of the corrosion inhibitor on the mechanical reservoir rock properties. This thesis aims to remedy this situation by performing compressive triaxial experiments on rock samples which have been saturated with inhibitor solutions. Two rock types which are representative of geothermal reservoir rocks were tested using two different inhibitors. The results were compared to a set of control experiments performed on water-saturated samples. The sandstone experiments show no discernible difference between the different fluid-types. The limestone experiments do show a number of differences: The limestone samples that were saturated with the first inhibitor type saw an increase in rock cohesion and a decrease in internal angle of friction. In contrast limestone samples that were saturated with the second inhibitor saw a decrease in rock cohesion and an increase in internal angle of friction. The lack of difference between the sandstone samples could be attributed to the inert nature of the constituent minerals. Limestone minerals are chemically more reactive and even though the exact nature of the chemical processes which lead to the observed differences remains unclear, a number of potential explanations are provided. We suggest that the change in mechanical rock parameters in the limestone rock are a result of the adsorption of the inhibitor components onto the particle surface. This adsorption alters the particle surface charge which leads to a change of the electrostatic repulsive forces. Additionally the same adsorption may affect the interparticle friction of our rock samples.

Acknowledgement

Since starting with my thesis I have received much support from many individuals. All of them have contributed in a significant way and I would therefore like to express my gratitude. To start I wish to express my gratitude to Peter Schorling and Bjoern Lause for providing the testing fluids without which this research would not have been possible. I would also like to thank Wim Verwaal and Ellen Meijvogel-de Koning for their help with generating the CT scans. I am also very grateful to Jolanda van Haagen-Donker for her help in creating the inhibitor solutions. I would also like to thank Mark Friebel, Jens van den Berg and Karel Heller for assisting me with my many questions. I am also very grateful to Milad Naderloo for helping me with cutting my rock samples. I wish to thank Auke Barnhoorn for his insights and feedback on my report and presentations. Additionally I would like to thank David Bruhn for taking place in my graduation committee. I would like to give a special thanks to Anne Pluymakers for giving me the opportunity to conduct this research as well as her tireless enthusiasm and her endless patience. I am very grateful for the many discussions we have had throughout the last few months. Finally I owe a deep appreciation to my friends and family for their continued support and encouragement.

Contents

1 Introduction

Geothermal energy is a renewable energy source. The production of geothermal energy releases fewer carbon emissions compared to the production of fossil fuels (e.g. Fridleifsson (2001)). As of June 2019, there were 18 geothermal sites in operation in the Netherlands and nearly all of those use corrosion inhibitor to protect the steel components from corrosion (van de Watering and van der Veld (2019)). One example of a developing geothermal project is the Delft geothermal project, which is often abbreviated as DAP: 'Delft Aardwarmte Project'. This project is aimed at providing geothermal energy to the campus of the Delft University of Technology by using geothermal wells targeting the Delft sandstone member. A comprehensive description of the depositional history of this formation is given by Van Adrichem Boogaert and Kouwe (1993). The DAP simultaneously serves as a research project that is aimed at increasing knowledge and understanding of geothermal energy production stichting DAP (2020). This project is of particular interest because it is associated to the faculty where this thesis was written.

From a hazard and operability analysis performed by van de Watering and van der Veld (2019) it was concluded that there is a risk of leakage of inhibitor solution into the geothermal reservoir. However there is a lack of information regarding any subsequent interaction between rocks and inhibitor fluids. This thesis is aimed at experimentally investigating what kind of influence the corrosion inhibitor has on the mechanical rock properties of the reservoir rocks. The above mentioned research goal will be addressed by the following research question:

What is the influence of corrosion inhibitor on mechanical rock properties?

The answer of the question above can then be evaluated in the context of inhibitor leakage during geothermal production:

What are the implications for the reservoir rock if inhibitor fluids were to leak into the reservoir?

The mechanical properties were tested by performing triaxial compressive experiments on a set of sandstones and limestones representative of reservoir rock. These rocks were saturated with either demineralized water or one of the two different inhibitor solutions. The results between the different sets were then compared.

2 Background information

This section provides a brief overview on three relevant topics to this thesis. The first subsection will contain some general information on corrosion inhibitors, which is the inhibitor type used in this research. The second subsection will provide some information on the topic of deformation and fracture mechanics in rocks. And the final topic will deal with the phenomena of surface charge that occurs when a solid comes into contact with a liquid.

2.1 Inhibitors

An inhibitor is defined by the Merriam-Webster dictionary (2020) as: "an agent that slows or interferes with a chemical action". The production of subsurface fluids in the petroleum and geothermal industry can be hindered by a number of (bio-)chemical production problems. A number of these problems are listed below:

- Microbial build-up Belyadi et al. (2019) & Croese (2018)
- Precipitation in the reservoir formation Belyadi et al. (2019)
- Fouling or scaling Belyadi et al. (2019) & Kelland (2014)
- Corrosion Belyadi et al. (2019) & Kelland (2014)

These problems can cause damage to the wellbore components and interfere with the production. The economic damage from scaling alone is estimated to be approximately 2 billion dollars per year, where the direct and indirect costs of corrosion are even greater Kelland (2014). Inhibitors form a cost effective solution to retard or prevent the aforementioned problems. Specific inhibitors exist to tackle one or several of these problems (Belyadi et al. (2019) and Kelland (2014)):

- *Biocide* prevents bacteria growth
- *Iron control* is the name of the additive which prevents precipitation of chemicals which could clog formations. It is added to the fracturing fluid in hydraulic fracking operations
- *Scaling inhibitors* prevent iron and scale accumulation in the formation and wellbore
- *Corrosion inhibitors* prevent corrosion of the wellbore components

In this thesis tests were conducted using corrosion inhibitors. The following section will provide some general information on these types of inhibitors.

2.1.1 Corrosion inhibitors

Corrosion is defined by Popoola et al. (2013) the destructive attack of a material by reaction with its environment. Several types of corrosion are distinguished, but in general corrosion involves localized anodic and cathodic reactions on the surface of the metal. This electrochemical redox process is described by Fayomi et al. (2019) " ... the water, acid or alkaline solution with dissolved species is aqueous in the environment. The liquid is a purely electrolyte-like corrosion process. This consists of two opposite but complementary reactions: oxidation (anodic reaction) and reduction (cathodic reaction). At the anodic site, the metal is oxidized or dissolved into the electrolyte while the cathodic reaction involves reduction of oxygen" The cathodic reaction depends on the acidity of the fluid, for a basic solution the reaction is given by reaction R1. In an acidic solution the cathodic reaction is given by reaction R2 and R3. The anodic reaction, which shows the oxidation of iron is given by reaction R4 and R5. To prevent this reaction corrosion inhibitors are used. A corrosion inhibitor is defined by Lingenfelder et al. (2018) as: “chemical substance that when present in the corrosion system at a suitable concentration decreases the corrosion rate, without significantly changing the concentration of any corrosive agent.”

$$\mathrm{O_2 + 2H_2O + 4e^-} \longrightarrow \mathrm{4OH^-} \tag{R1}$$

$$\mathrm{2H^+ + 2e^-} \longrightarrow \mathrm{2H} \tag{R2}$$

$$\mathrm{H + H} \longrightarrow \mathrm{H_2} \tag{R3}$$

$$\mathrm{Fe} \longrightarrow \mathrm{Fe^{2+} + 2e^-} \tag{R4}$$

$$\mathrm{Fe^{2+} + 2OH^-} \longrightarrow \mathrm{Fe(OH)_2} \tag{R5}$$

The application of corrosion inhibitors is widespread across many different fields. Applications range from material treatment in chemical and industrial sectors to surface treatment for monuments and cultural heritage sites. Lingenfelder et al. (2018) Different types of corrosion inhibitors are aimed at interrupting this process. They are classified based on their operation Kelland (2014)(Although other authors may use different classification systems e.g. Lingenfelder et al. (2018)). The first three corrosion inhibitors below are not often used in a geothermal production setting, the final category of inhibitors is widely applied in the Dutch geothermal sector (van de Watering and van der Veld (2019)):

- **Passivating** corrosion inhibitors form a nonreactive thin surface film on the metal which inhibits corrosion. They are not used in high salinity environments such as oil and gas production.
- **Cathodic** inhibitors reduce the corrosion by hindering the reduction of water to hydrogen gas. These inhibitors are also not commonly used in a production environment. Kelland (2014).
- **Volatile** inhibitors will travel to the metal surface by gas diffusion and form a protective barrier to corrosive elements. The inhibitor is attracted to the anode and cathode of the metal. This type of inhibitor is sometimes applied in the production of wet gas.
- **Film forming** inhibitors adsorb to the metal surface and form a protective barrier that physically prevent corrosive chemicals from penetrating. McMahon (1991) Many film forming corrosion inhibitors are organic amphiphiles (surfactants) with a nitrogen based polar headgroup (which interacts with the iron atoms on the surface) and an apolar carbon based hydrophobic tail (e.g. van de Watering and van der Veld (2019)) The tails will generally attract liquid hydrocarbons, forming an oily film to form an additional barrier to the corrosive elements. (See figure 1) Kelland (2014). Depending on the inhibitor and the dosage the hydrophobic tails may self-assemble to form a double layer as shown in figure 2 Only film forming corrosion inhibitors are currently applied in the Dutch geothermal sector. They are continuously injected in the production well, at a depth just above the reservoir level (van de Watering and van der Veld (2019)).

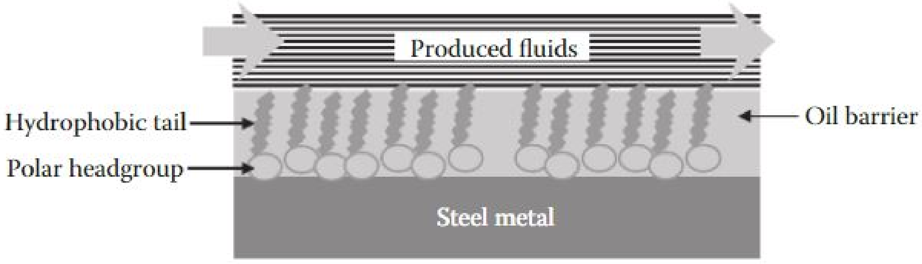

Figure 1: Operation of a film forming corrosion inhibitor Source: Kelland (2014)

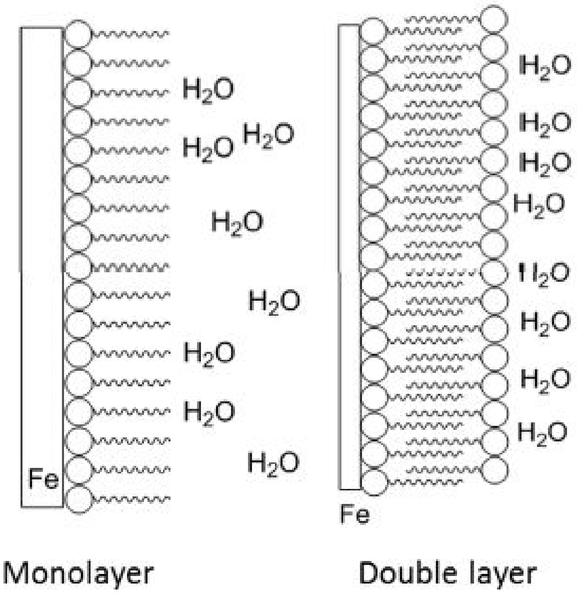

Figure 2: Depending on the inhibitor properties and the applied dosage the inhibitor molecules may self-assemble in a monolayer or a double layer. (Source: van de Watering and van der Veld (2019))

2.2 Rock deformation

As rocks are subjected to stress they tend to deform. The experiments conducted for this thesis will seek to deform the rocks until they break. When rocks break they are said to fracture. A fracture (also known as a crack) is defined by Fossen (2010) as: "... any planar or subplanar discontinuity in displacement and mechanical properties." Fractures are characterised by a reduction or complete loss of cohesion. They are formed as a result of stress. Two deformation endmembers are distinguished in the material sciences: Brittle fractures (e.g. Sun and Jin (2011); Perez (2016)) and ductile deformation (e.g. Fossen (2010)). Brittle fractures form abruptly after minimal plastic deformation. Although some materials will show a substantial amount of ductile deformation prior to fracturing. In this case the fractures are described as brittle-ductile fractures. In general rocks tend to behave more ductile as temperature and confining pressure are increased. (e.g. Fossen (2010); Jaeger et al. (2009)) This is illustrated in figure 3.

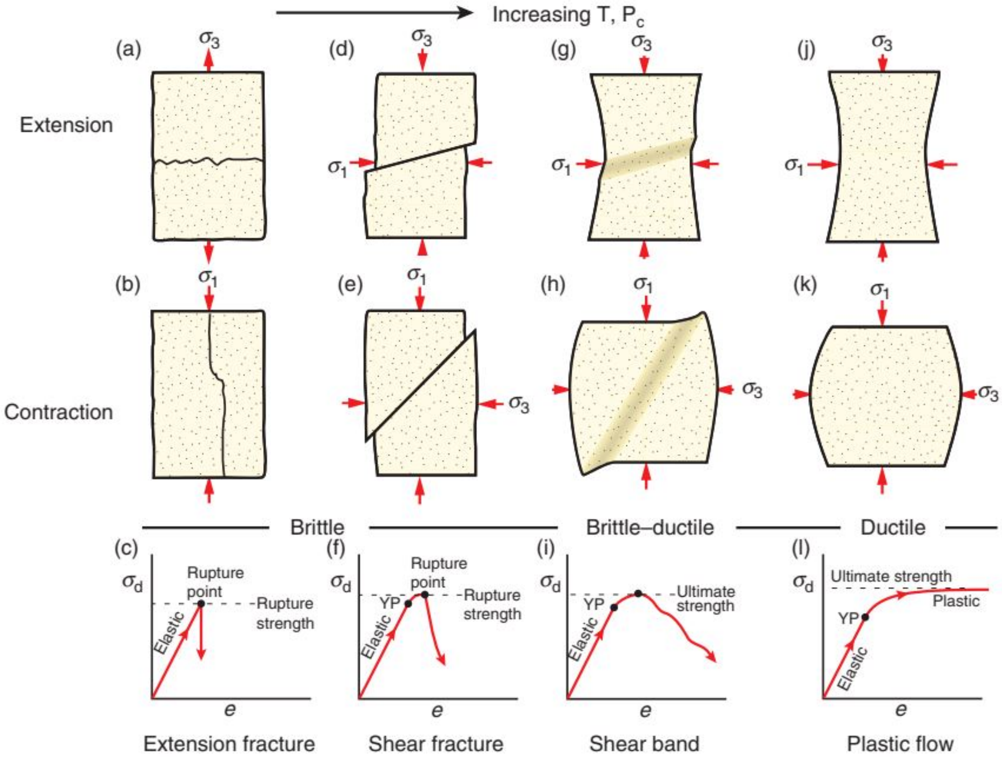

Figure 3: Deformation structures will vary with temperature and pressure Fossen (2010)

In addition it is also common to classify the displacement field of the fractures into different modes such as described by Fossen (2010):

Mode I is called 'opening' or 'extension mode'. Here displacement is normal to the walls of the crack.

Mode II is called 'sliding mode'. Here displacement is parallel to the the walls of the crack and perpendicular to the edge of the crack.

Mode III is called 'tearing mode'. Here displacement is parallel to the walls of the crack and parallel to the edge of the crack.

Mode IV is called 'closing mode'. This term is used to describe features such as stylolites or dissolution seams (e.g. Toussaint et al. (2018)) , which are of a contractional nature.

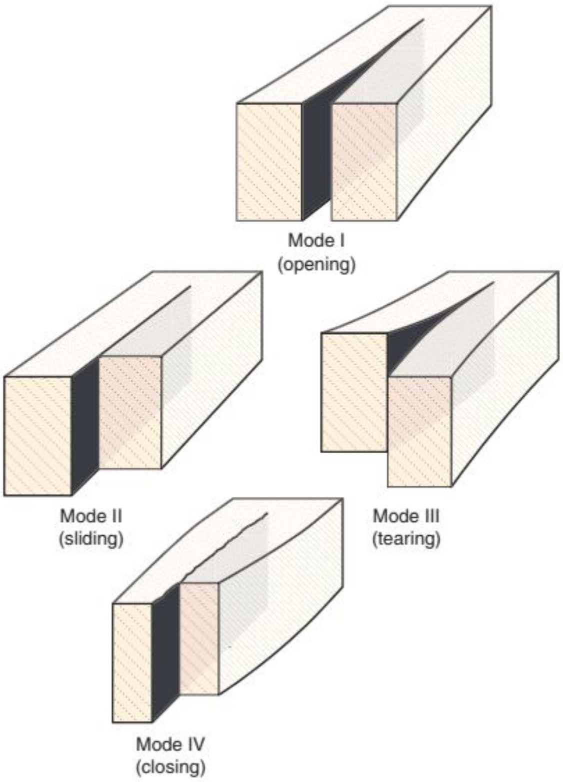

Figure 4: Illustration showing the different fracture modes. Source: Fossen (2010)

Mode I fractures can be associated with either tensile stress or compressional stress. In the case of tensile stress the fracture will develop perpendicular to the direction of the tensile stress. Mode I fractures typically only develop in a compressional regime if there is a low or no confining pressure. In this scenario the fracture will develop parallel to the direction of the maximum principal stress. Mode II and III fractures are referred to as shear fractures. Shear fractures typically develop in a direction oblique to the maximum principal stress. The relative movement (or slip) of the fracture surfaces is parallel to the fracture plane. In an experimental setting shear fractures often occur in conjugate pairs, however it is mentioned by Paterson (1978) "that this may be an experimental artifact caused by the ends of the specimen being constrained against rotation." Researcher Alan Arnold Griffith has studied brittle deformation in rocks. His theory named *Griffith's theory of fracture* states that microscopic cracks, pores and other flaws control the brittle strength of a rock. The theory is based on the assumption that these flaws (which are normally present in natural rocks) grow and link together under the influence of the stress field. The growth of the micro-cracks and flaws can be explained by the fact that the stress is concentrated at the tips of these discontinuities as illustrated in figure 5. As these flaws grow, they link together with other flaws to form macroscopic fractures. This theory is supported by the relatively high amount of microfractures observed near macroscopic fractures. Fossen (2010) This area with these high amounts of microscopic fractures is called a process zone, and according to the Griffith theory the process zone forms ahead of a macroscopic fracture. In this process zone the microfractures with the orientation close to that of the maximum shear stress (or perpendicular to the minimal stress) will encounter the most stress, and are therefore expected to grow fastest and link together as illustrated in figure 6.

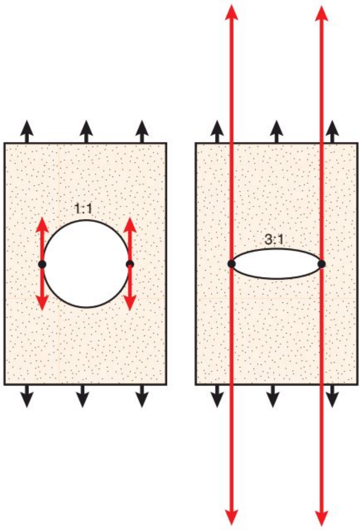

Figure 5: Image and description from Fossen (2010) "Illustration of local stress concentration in a material with a circular and an elliptical hole. If the material is a sheet of paper it means that the paper with the elliptical hole will be easier to pull apart. Black arrows indicate the remote stress"

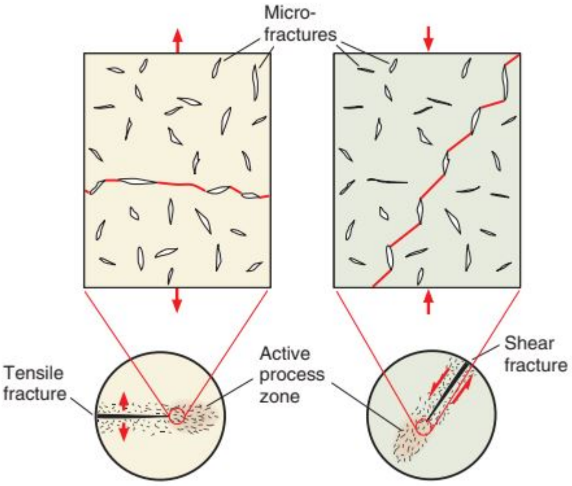

Figure 6: Image and description from Fossen (2010): "Simplified illustration of growth and propagation and linkage of tensile microfractures (flaws). Propagation occurs in a process zone in front of the fracture tip. Circled figures are centimeter-scale view while rectangular views illustrate the microscale structure."

2.3 Surface charge

When a solid is exposed to a liquid, the interface between the two phases is almost always marked by a separation in electric charges. On the surface of the solid phase there will be a charge of one sign and a balancing charge will be present in the adjoining surface of the liquid phase (e.g. Hunter (2013)). There forms a structure of two parallel layers of charge on the surface of both phases which is referred to as the electric double layer. The first layer consists of ions adsorbed to the surface due to chemical interaction. This layer is also known as the Stern layer after Otto Stern. He proposed the theory that ions could be adsorbed to the surface of the solid phase. The Stern layer is immobile with respect to the solid phase its thickness is in the order of 1 nm. The potential charge of the Stern layer attracts the second layer of free ions via the Coulomb force. This layer is called the diffuse layer. The thickness of the diffuse layer may extent up to 10 nm (Zhong et al. (2018)). The diffuse layer essentially balances out the potential charge to the equal that of the bulk fluid. This is schematically illustrated in figure 7. A part of the fluid of the diffuse layer is immobile and will remain attached to the surface under a tangential stress. This immobile part of the diffuse layer, together with the immobile Stern layer are separated from the mobile fluid by the surface of shear, also called the slipping plane (Morrison and Ross (2002)). The electrical potential at this slipping plane is called the zeta potential (denoted as ζ). ζ is considered a better indication for the degree of electrostatic repulsion between similarly charged particles than the surface charge (Hunter (2013)). The zeta potential is affected by the liquid pH value, temperature, ionic strength and concentration of additives (e.g. Lu and Gao (2010)). In the context of this thesis it is worth noting that there is a difference in the surface charge for limestones and sandstones. As mentioned before, the surface charge and ζ are also influenced by fluid properties and temperature, but in general it seems that: For sandstone the surfaces are negatively charged (e.g. Shehata et al. (2015); Hilner et al. (2015)). For limestone rocks it is known from Bassioni and Taha Taqvi (2015) that "carbonated reservoir rocks, consisting of $CaCO_3$ mainly, are positively charged and their surface has the potential to adsorb significant quantities of anions."

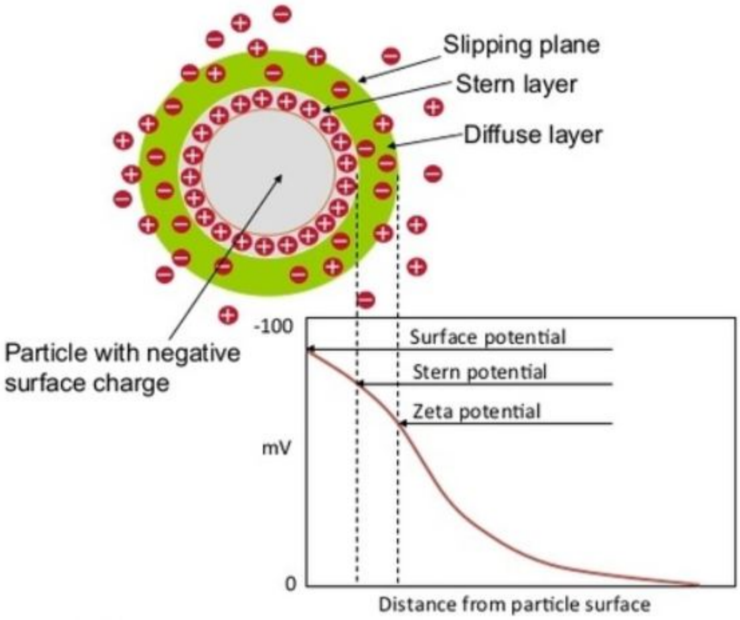

Figure 7: Diagram showing the ionic concentration and potential difference at phase interface, as a function of distance from the charged surface. (Source: analytik.co.uk (2020))

3 Methodology

A series of compressive triaxial tests were performed on a selection of cylindrical rock samples consisting of limestone and sandstone rocks. The rock specimen, were saturated with one of three different fluids in order to test how the rock strength behaviour was influenced by these pore-fluids. In this type of axisymmetric triaxial test, a hydrostatic pressure acts on the samples radially as the confining pressure, and an axial load is superposed on the rock parallel to the length direction of the sample. In one series of experiments four rock samples are tested. All of the rock samples belonging to the same series were saturated with the same type of fluid. The saturated samples were then loaded under an increasing axial load until failure occurred. The axial loading took place, whilst the samples were exposed to a radial confining pressure of 10, 20 or 30 MPa. A repeat experiment was performed for the confining pressure of 10 MPa.

3.1 Material Description

For the compressive strength experiments two type of rocks were used: The Bentheim sandstone and Treuchtlinger marmor. These rocks are representative of the wide variability of the rocks which are encountered in the production of geothermal reservoirs. The Bentheim Sandstone is a member of the Vlieland Sandstone formation. This sandstone is named after the German town Bad Bentheim, where this rock has been quarried as a building material since the beginning of the 12th century Dubelaar and Nijland (2015). This formation is of Early Cretaceous (Valanginian) age. It was deposited in the Western Part of the Lower Saxony Basin, in a coastal (deltaic) to shallow marine environment Boogaert and Kouwe (1993). Literature descriptions of the rock vary somewhat depending on the author. For instance the composition of the rock has been described by Klein and Reuschlé (2003) as: 95% quartz, 3% kaolinite, and 2% orthoclase. Whereas the composition given by Peksa et al. (2015) mentions: 92% quartz, 5% feldspars, 3% clay minerals and $<$1% pyrite and iron minerals. The Bentheim Sandstone forms an important reservoir rock for several oil and gas fields in the Netherlands and Germany.

The Treuchtlinger Marmor (also known as Jura-Marmor, Jura-Kalkstein and Treuchtling Marble) is the second rock-type on which the triaxial compressive experiments were conducted. The name "Treuchtlinger Marmor", which originates from the German village of Treuchtlingen, is actually a misleading brand-name as this rock is not of metamorphic but sedimentary origin Niebuhr and Pürner (2014). The Treuchtlingen formation belongs to the Late Jurrasic (Middle Kimmeridgian, also known as the White Jura) Mönnig (2006). This rock is a light-yellow to blue-grey fossil-rich, fine-grained limestone. It is characterised by thick and well-bedded silicate-sponge biostromes with abundant Tubiphytes Koch and Weiss (2005). The Treuchtlinger Marmor samples used in this experiment were gathered as analogue samples for the geothermal target Upper Jurassic carbonate rock in the southwest Bavarian Molasse Basin in Germany Tamaskovics et al.. The samples have been gathered in the area of Inglostadt.

3.2 Experimental Set-Up

The testing equipment consisted of the main loading apparatus, which is a servo-controlled uniaxial loading machine powered by an external pump. The produced force is measured by an internal load cell with a range of 500 kN. Inside the uni-axial loading frame a Hoek triaxial cell was placed. The Hoekcell consists of a cylindrical steel body, with a quick release self-sealing coupling for oil inlet, two steel end caps which are screwed to the cell body, a rubber sealing sleeve to separate the specimen from the cell fluid. The rock samples were placed within this rubber sleeve inside the Hoekcell. An external direct displacement syringe pump (ISCO 65D) controls the fluid pressure on the outside of the sleeve to superpose a confining pressure on the rock specimen. In order to position the rock sample within the Hoekcell a set of top and bottom end-caps are used. Both the top and bottom cap are perforated to prevent pore-pressure build-up. One end of each end-cap is dome-shaped, and was connected with a spherical seat to ensure vertical sample alignment. Piston displacement was measured using two high-precision linear variable differential transformers (LVDT).

3.3 Experiment Preparation

Core samples from the rock types described in section 3.1 were used for testing. These cores had a cylindrical shape with a length of approximately 60 mm and a diameter of 30 mm. The effective porosity of the samples was determined using a gas pycnometer. Gas pycnometry can be used to determine the volume of solid particles of an object of interest. This procedure is based on Boyle-Mariotte's Law and is described in greater detail in appendix A.

The limestone samples that were selected for testing had measured porosity values that ranged from 7.7% to 10.3%. Some of these samples showed small features, such as thin styllolites or slightly chipped edges. A descriptive overview of the selected limestone samples is given in table 1. The selected sandstones samples were more uniformly looking and exhibited no significant features or structures. The sandstone porosity ranged from 26.0% to 27.3%. An overview of the selected sandstones samples is shown in table 2. To prepare the samples for testing, the ends of all selected samples were ground with silicon carbide powder until they were plane-parallel within 100 μm. The polishing step left trace amounts of residual silicon carbide powder on the sandstone rock-samples.

The experiments were performed with one of three fluids. A set of control experiments was performed using demineralised water (resistivity of 18.2 MΩ.cm at 21.8°C). The other experiments were conducted using one of two different corrosion inhibitors, which were provided trough the courtesy of Baker-Hughes. The corrosion inhibitors were provided under the condition that their contents would not be analysed. So the chemical components of the inhibitors are undetermined. However it is known that these types of corrosion inhibitors are commonly used in the Dutch geothermal industry, where they are continuously added in production wells at a concentration between 4 - 15 ppm (e.g. van de Watering and van der Veld (2019)). For the purpose of these experiments, a higher dose of 3000 ppm was used. This concentration was accomplished in two steps of weight-based dilution of the pure inhibitor with demineralised water. First 10 g inhibitor was mixed with 90 g demineralised water. From the resulting mixture, 30 g was mixed with 870 g of demineralised water.

Prior to conducting the triaxial compressive test, the rock samples were saturated with the testing fluid. The samples were placed in a cup which was then filled with testing fluid so that the samples were submerged. The cups where then placed in a vacuum desiccator at a residual pressure of -1 bar. Each sample was left under vacuum for a period of 30 minutes. After this period the cups containing the samples and the fluid were taken out of the desiccator. The cups were then sealed and left overnight.

Selection of limestone samples			
Sample	**Porosity [%]**	**Std. [%]**	**Sample features**
TM3-6	8.8	0.16	Thin styllolites (running lengthwise)
TM4-2	10.3	0.12	Sound sample without any visible flaws
TM4-1	10.2	0.13	Sound sample without any visible flaws
TM2-4	8.3	0.24	Thin styllolites (running lengthwise)
TM2-8	8.3	0.19	Thin styllolites (running lengthwise), small corner chipped of the top
TM2-2	7.8	0.12	Thin styllolites (only visible in the top and bottom edge), small corner chipped off the bottom
TM2-5	8.8	0.13	Thin styllolites (running lengthwise), small corner chipped off the bottom
TM3-3	7.8	0.09	Thin styllolite (visible in the top edge)
TM2-7	8.7	0.17	Thin styllolites (running lengthwise), chipped corner off the bottom
TM2-6	7.7	0.23	Thin styllolites (running lengthwise)
TM2-3	8.5	0.11	Small corner chipped off the bottom
TM3-1	8.3	0.12	Sound sample without any visible flaws

Table 1: Overview of the limestone samples selected for testing

Selection of Sandstone samples			
Sample	**Porosity [%]**	**Std. [%]**	**Sample features**
BS-05	26.5	0.47	Sound sample without any visible flaws
BS-09	26.9	0.47	Sound sample without any visible flaws
BS-07	26.7	0.47	Sound sample without any visible flaws
BS-12	26.6	0.42	Sound sample without any visible flaws
BS-04	26.0	0.30	Sound sample without any visible flaws
BS-01	26.8	0.18	Sound sample without any visible flaws
BS-10	27.3	0.46	Sound sample without any visible flaws
BS-11	26.7	0.32	Sound sample without any visible flaws
BS-17	27.1	0.39	Sound sample without any visible flaws
BS-16	26.6	0.38	Sound sample without any visible flaws
BS-15	27.2	0.46	Sound sample without any visible flaws
BS-14	26.6	0.33	Sound sample without any visible flaws

Table 2: Overview of the sandstone samples selected for testing

3.4 Testing procedure

After the saturation period the sample was placed inside the Hoekcell. The Hoekcell with the loaded sample were then mounted in the loading frame. Once the Hoekcell was in place the LVDT's were placed and the recording was started. The confining pressure and axial load were then slowly built up. The axial load was kept 1 kN above the confining pressure. Once the targeted confining pressure was reached the experiment could begin.

During the experiment the sample was loaded at a constant displacement rate such that the axial strain rate was 8.33×10^{-6} as measured on the LVDT's. During the experiment the relative piston displacement, the axial force, the confining pressure and the fluid flow-rate from the ISCO pump (among other variables) were logged at 1 second intervals. The radial pressure was generated by the ISCO pump. Loading continued until the measured axial load started dropping abruptly. This abrupt drop in load was interpreted as the point where macroscopic fractures formed and the rock failed. To prevent any further displacement and possible risk of damaging the Hoekcell sleeve, the piston movement was reversed.

The unloading process followed a similar but opposite procedure as the one described for the loading process. Here the axial load was kept the equivalent of 5 kN above the confining pressure. Once a confining pressure of 3 bar was reached, the axial load was completely released, and the assembly was taken out of the loading frame. The confining pressure was then fully released at which point the sample was removed from the Hoekcell.

Some samples were still coherent when they were removed from the Hoekcell. Some samples including most sandstone specimen broke during testing or when they were removed afterwards. Any resulting rock debris was cleaned from the Hoekcell. After every test run, any part that had been in contact with the chemical pore-fluid, was cleaned using ethanol.

3.4.1 Computed Tomographic Analysis

We obtained post-experimental 3D micro-tomography scans of selected samples. This was done to provide an additional basis to study and compare the selected samples. Computed Tomography (CT) is described by Vicente et al. (2017b), Wolański et al. (2017) and Ji et al. (2014), as a non-destructive 3D imaging technique. The images consist of computer-processed combinations of many x-ray measurements. These measurements are obtained in a CT-scanner, which is equipped with an emitter and a detector. The emitter releases x-ray signals trough the object of interest. As the signal travels trough the object, a part of the signal energy is absorbed by the material, after which a detector measures the intensity of the x-ray. The degree of attenuation is dependent on the material density along the trajectory. By emitting and capturing the x-ray from multiple angles, it is possible to compute a 3D virtual micro-structure of the scanned object. This 3D structure is visualised as thin cross-sectional slices. These slices are built from data-points called voxels. Each voxel is assigned a grey-scale value that corresponds to the density value of the object in place. For the images in this thesis, the lighter shades represent higher density values. The scans were made and pre-processed at the Laboratory of Geoscience and Engineering at the faculty of Geosciences and Civil Engineering of the Delft University of Technology. A Nanotom scanner, that operates at a voltage of 180 kV and a current of 0.5 mA was used to generate the images. Full and half resolution images were made, at full resolution the images have a voxel size of $(28\ \mu m)^3$. At half resolution the images have a voxel size of $(56\ \mu m)^3$. At the latter resolution the processed scans consist of around 1150 slices of 550 × 550 voxels. The following samples were scanned: BS-17 (full resolution), TM2-4 (half resolution), TM2-5 (half resolution) TM2-8 (full resolution) and TM3-6 (full resolution). The resulting images are analysed and described qualitatively in section 4.3.1. The Fiji 2012 distribution of ImageJ was used perform the analysis. The fractured sample description is based on 2-D vertical and horizontal slices. The images shown in section 3.4.2 are selected to give the reader a clear view of the fracture pattern. The fracture aperture was measured in the horizontal slices. In addition a more quantitative approach was attempted to obtain statistical information about the fracture openings. For this method the aperture was measured at regular intervals on equidistant horizontal slices. The results of this method are shown separately in appendix B for reasons mentioned in the appendix and in section 5.

Several authors (such as Chakraborty et al. (2019), Basu et al. (2013) and Szwedzicki and Shamu (1999) have described and categorized the failure patterns or fracture modes for compressive laboratory experiments. For the experiments described in this thesis, a selection of the failure modes described by Szwedzicki and Shamu (1999), sufficiently covers encountered failure patterns (see figure 8). A *simple shear* fracture is characterized by a failure along one plane (or multiple parallel planes) situated at an oblique angle to the direction of maximum compression. For *multiple shear* the failure occurs along multiple planes situated at an oblique angle to the direction of maximum compression, but not parallel to each other. For *multiple fracture* the the failure takes place along many planes in random directions.

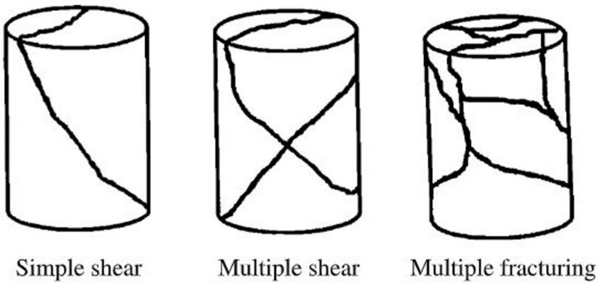

Figure 8: Schematic overview of a selection of the different failure modes. (Image modified from : Szwedzicki and Shamu (1999))

3.4.2 Thin section petrography

Petrographic analysis of thin sections is a laboratory technique used to study rock samples. This technique involves glueing a sample to a glass plate, grinding the rock samples to a thickness of 30 µm and then polishing the sample. The optical properties of the samples can then be studied under a polarizing petrographic microscope. For this thesis thin section analysis provides an additional means of comparing the different rock samples detail. The samples that were analysed this way are: BS-09, TM2-2 and TM4-2. A qualitative description is provided in section 3.4.2. Note that, due to COVID-19 restrictions, the analysis presented here is limited to a low magnification scan taken of the thin sections.

3.5 Data processing

In line with the convention proposed in Jaeger et al. (2009), this paper will define compressive stress and compressive axial strain as positive. The principal normal stresses are denoted as σ_i, with $\sigma_1 > \sigma_2 = \sigma_3 = P_c$ where σ_1 is the axial stress and P_c is the confining pressure. The *differential stress* is denoted as $\sigma_{diff} = \sigma_1 - \sigma_3$. The *rock strength* is defined as the peak differential stress $(\sigma_{diff})_{max}$. This value is also referred to as the *compressive strength* of the rock is defined as the maximum axial stress value the sample can withstand before failure and is denoted as C_i, where the subscript i corresponds with P_c. For example, C_{20} is the compressive rock strength that was found for a sample that was subjected to a confining pressure P_c of 20 MPa The *axial strain* is the ratio of the change in sample length over the original sample length. The axial strain is denoted as $\epsilon_1 = dL/L_0$. The sample strain that is measured at the maximum axial stress is called the *peak stress strain* which is denoted as ϵ_p. The linear part of the stress - strain curve is used to determine the *Young's Modulus* (denoted as E), which is calculated by:

$$E = d\sigma_1/d\epsilon_1. \tag{1}$$

The linear interval of the curve was selected manually for the purpose of calculating the Young's Modulus. The sample *yield strength* is defined as the value of the differential stress at which the differential stress vs. the axial strain curve deviates from linearity. Finally this paper uses the term *ductility* on par with the definition that is given by Handin and Hager (1957): Ductility is the total strain before (macroscopic) fracture. The experimental data can be applied to predict when and how rocks fail under the action of external loads. For this paper the Mohr-Coulomb failure criterion, also described in Mehranpour and Kulatilake (2016), was chosen to characterize the experimental results. It has proven to be a suitable failure criterion for this set of experiments. This criterion is defined by the following equation:

$$|\tau| = S_0 + \mu\sigma \tag{2}$$

Here τ is the *shear stress*, S_0 is a rock parameter known as the *cohesion*, μ is known as the coefficient of friction. The state of stress can be visually represented in a Mohr diagram (also known as a Mohr half-circle) plotted on the σ - τ plane. The left intersection of the Mohr-half circle with the horizontal axis represents the value of σ_3 and the right intersection represents the value of σ_1. In figure 9 the line A-L represents the Mohr-Coulomb failure criterion (eq: 2). As long as the Mohr-circle lies below the failure criterion, the state of stress does not give rise to rock failure, if the circle touches the failure criterion, failure will occur.

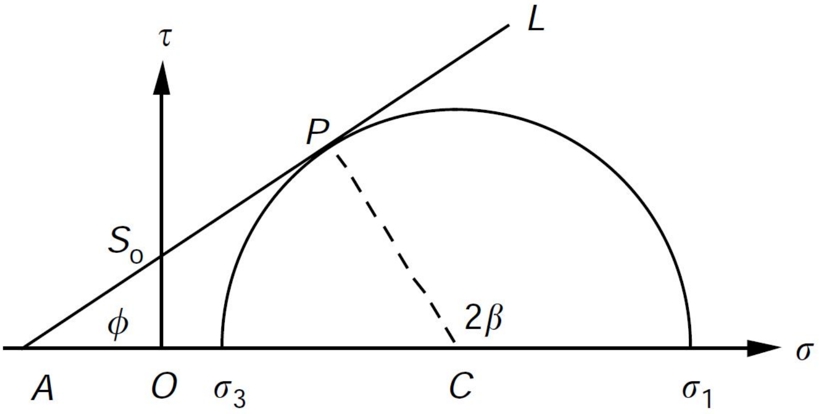

Figure 9: Visual representation of the Mohr-Coulomb failure criterion, modified from: Jaeger et al. (2009) The line A-L represents the Mohr-Coulomb failure criterion. The Mohr-half circle represents the state of stress. The tangency point P is where the circle will first touch the failure criterion. β represents the angle of the failure plane. ϕ is the Angle of (internal) friction, which is the tangent of the coefficient of friction: $\tan\phi = \mu$

To construct the Mohr-Coulomb failure envelope from the experimental data, trigonometry is used to obtain the tangency points. By connecting the tangency points of two Mohr half-circles, a single failure criterion is constructed. This failure criterion can be expressed as a linear equation (equation: 2). To extend this method to apply for more then two experiments, the tangency points are calculated for all sets of two experiments. The Mohr-Coulomb failure envelope is the arithmetic mean of all the resulting linear equations. The methodology is explained here using two experiments called experiment A and experiment B resulting in σ_{1A}, σ_{3A}, σ_{1B} and σ_{3B}. Then the centers of the circles obtained by:

$$C_i = \frac{\sigma_{1i} + \sigma_{3i}}{2} \tag{3}$$

The distance D between the center of the two circles is calculated by:

$$D = |C_a - C_b| \tag{4}$$

The radii of the circles are obtained by:

$$r_i = \frac{\sigma_{1i} - \sigma_{3i}}{2} \tag{5}$$

The unit vectors that start at the center of the circle and points towards points P_i can then be constructed:

$$\vec{u} = [-\frac{r_b - r_a}{D}, \frac{\sqrt{d^2 - (r_b - r_a)^2}}{D}] \tag{6}$$

With this unit vector the tangent points P_i can be determined with:

$$[P_a] = C_a + r_a \times \vec{u} \tag{7}$$

$$[P_b] = C_b + r_b \times \vec{u} \tag{8}$$

The vector connecting points P_a and P_b then forms the outer tangent line of the two Mohr half-circles. This line is then extended beyond the tangent points to form the Mohr-Coulomb failure criterion. The extended tangent line is expressed as a linear equation, which equals equation 2.

3.5.1 Weight based porosity calculation

To obtain the sample porosity after fluid saturation a weight based porosity calculation was used. This was done because the pycnometer can't be applied on saturated samples. The weight based porosity calculation is based on equation 9. Here V_p is the pore volume, V_b is the bulk rock volume, m_f is the fluid mass, which is found by taking the difference of the sample mass prior to saturation and the saturated sample mass. Finally ρ_f is the fluid density.

$$\phi = \frac{V_p}{V_b} = \frac{\frac{m_f}{\rho f}}{V_b} \tag{9}$$

The results of this method turned out to be inaccurate. As such it was impossible to use this method to check if any porosity changes had occurred. This inaccuracy can be explained by two shortcomings: First of all in this calculation the rock mass and the fluid density are considered constant. This is only true if no rock material is dissolved. If the other hand rock material dissolves this will increase the fluid density due to an increase in dissolved material at the same time the rock mass will decrease. The second shortcoming of this method stems from the difficulty of accurately measuring the saturated sample. When the wet sample is taken out of the cup the fluid will not only be inside the pores, but it will also form a thin film on the outside of the sample. When drying this outside film, there is a risk of absorbing some of the pore fluid from the sample.

3.5.2 Experiment repeatability

According to Jaeger et al. (2009) mechanical properties of a rock vary between different rock types but also between different specimens of nominally same rock. This is due to differences in the arrangement or composition of mineral grains, the presence of (micro-)cracks and other heterogeneities introduced during the long geological history. As a consequence of this inherent rock variability, repeat experiments were performed to give a measure of spread of the experimental results. To this end the *range* (eq: 10) and *variance* (eq: 11) are used. The range is defined by Triola (2014) as "the difference between the highest sample value and the lowest sample value". The range can be determined for the mechanical properties for each rock type. It is denoted as R_x, where the subscript x represents the property of interest. For example: R_C represents the range of the compressive rock strength.

$$R_x = x_{max} - x_{min} \tag{10}$$

Where x_{max} and x_{min} are the maximum and minimum observed values of the rock property. The variance is defined by Isaaks et al. (1989) as "the averaged square difference of the observed values from their mean". In this paper it will be denoted as v_x^2.

$$v_x^2 = \frac{1}{n}\sum_{i=1}^{n}(x_i - m)^2 \tag{11}$$

Where n is the number of experiments, and m is the mean value of the experiment variable. Additionally a *coefficient of the range* (eq. 12) is proposed to facilitate the comparison between experiment results. This coefficient will be denoted as r_x and will also be referred to as the *experiment repeatability.*

$$r_x = \frac{R_x}{m} \tag{12}$$

4 Result

All experiments show that an increased confining pressure results in an increased rock strength. Additionally the amount of axial strain a sample can endure before failure is also increased for higher confining pressures. Similar trends were expected: For sandstones this increase in strength with confining pressure is also described by Yang et al. (2012) for red sandstone and in Heap et al. (2009) for Darley Dale sandstone. For limestones this increase in strength at higher confining pressures is described by Rutter (1972) for Solenhofen limestone and You (2010) describes this relationship for the Solenhofen, Indiana and Tyndall limestone.

Rock type	Liquid	P_c [MPa]	Sample	ϕ [%]	C_i[MPa]	E [GPa]	ϵ_p [%]	S_0	μ
Sandstone	Water	30	BS-05	27	177	25	1.02	20 ± 3	0.8 ± 0.1
		20	BS-09	27	149	24	0.85		
		10	BS-07	27	110	24	0.65		
	Inhibitor 1	30	BS-04	26	174	25	1.03	19 ± 3	0.8 ± 0.1
		20	BS-01	27	145	24	0.79		
		10	BS-10	27	107	22	0.65		
		10	BS-11	27	111	23	0.67		
	Inhibitor 2	30	BS-17	27	177	25	1.00	18 ± 3	0.8 ± 0.1
		20	BS-16	27	146	25	0.81		
		10	BS-15	27	110	23	0.67		
		10	BS-14	27	109	23	0.66		
Limestone	Water	30	TM3-6	9	206	50	0.57	35 ± 5	0.7 ± 0.1
		20	TM4-2	10	180	43	0.55		
		10	TM4-1	10	153	44	0.47		
		10	TM2-4	8	157	50	0.35		
	Inhibitor 1	30	TM2-8	8	217	47	0.66	59 ± 9	0.4 ± 0.1
		20	TM2-2	8	202	39	0.59		
		10	TM2-5	9	191	47	0.54		
	Inhibitor 2	30	TM2-6	8	242	53	0.74	21 ± 3	1.0 ± 0.1
		20	TM2-3	9	206	45	0.56		
		10	TM3-1	8	147	39	0.47		
		10	TM2-7	9	148	45	0.38		

Table 3: An overview of the test results

4.1 Sandstone

The mechanical parameters obtained from these experiments are listed in table 3. The results of the triaxial test are also visualised in a differential stress - strain plot, where the differential axial stress is plotted on the vertical axis and the axial strain is plotted on the horizontal axis. Figure 10 shows the stress-strain curves divided into three sets. The rocks that were saturated to the same liquid are grouped together and shown in the same plot. Generally speaking, for strain-controlled compression experiments, rock failure is marked by an abrupt drop in the axial load. For all confining pressures tested and for all fluid types, the sandstone experiments resulted in brittle fracture. From the repeat experiments the range R_c for the sandstone rock strength is 4 MPa, giving a repeatability r_c of 4%. The variation of rock strength between the different fluids is within this 4%. So it is concluded that there is no measurable difference in the rock strength for the sandstone samples saturated with inhibitor 1 or inhibitor 2 compared to water. The largest value C_{30} is 177 MPa, for C_{20} and C_{10} these values are 148 and 111 MPa respectively. To analyse the impact of the fluid-type on E and ϵ_p these parameters are plotted against P_c as shown in figures 11 and 12. The values for the sandstone Young's modulus range from 21.6 to 25.1 GPa. Based on the repeat experiments the r_E equals 7 %. When considering this experiment repeatability the Young's modulus of the sandstone is not affected significantly by the different fluid types. The values for ϵ_p range from 0.065 to 0.102. This value increases considerably with an increase in P_c. The values for ϵ_p show no appreciable difference between the different sandstone batches. The r_{ϵ_p} equals 3 %.

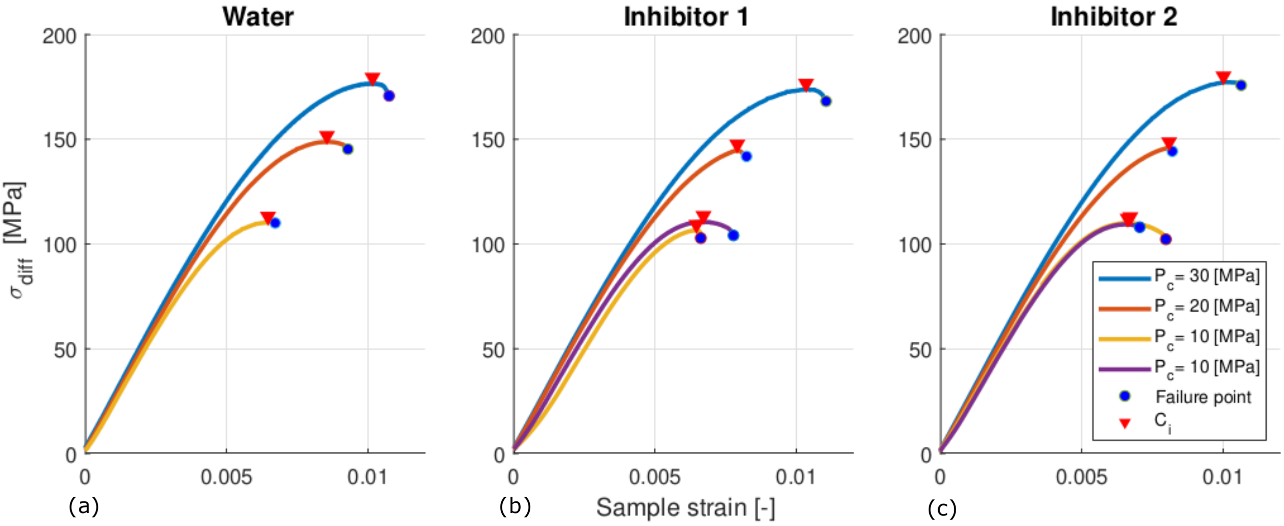

Figure 10: Differential stress-strain curves for the triaxial compressive tests performed on sandstones saturated with (a) water, (b) inhibitor 1 and (c) inhibitor 2. The *failure point* marks the location where the axially supported load on the sample was rapidly declining. This was where the loading process was stopped and unloading began. The C_i markers indicate the peak axial stresses.

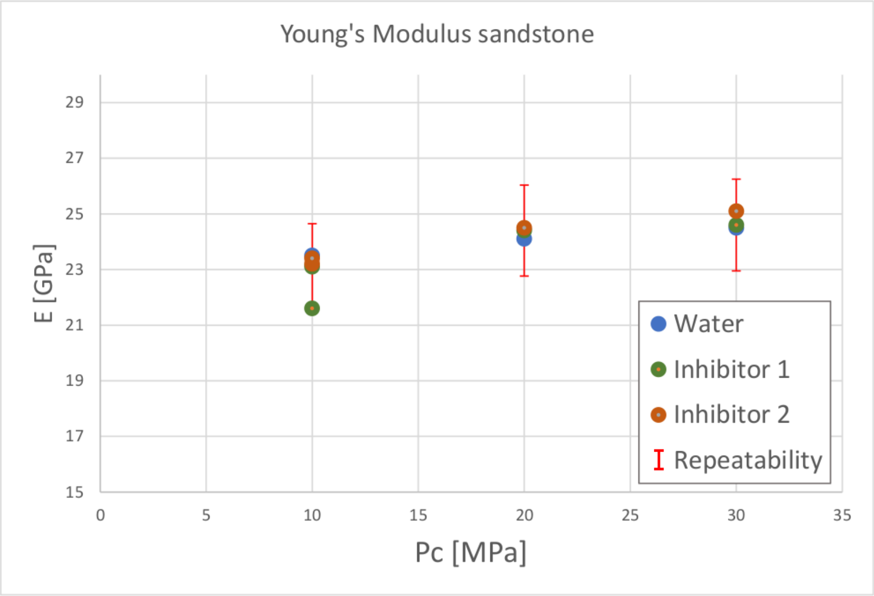

Figure 11: The sandstone Young's Modulus is plotted against the confining pressure. The experiment repeatability is shown as an error bar. Note that the error bar is only plotted around the inhibitor 1 values. This is done solely to keep the image clear and readable. From the experiment results no relation between pore fluid and the Young's Modulus was established.

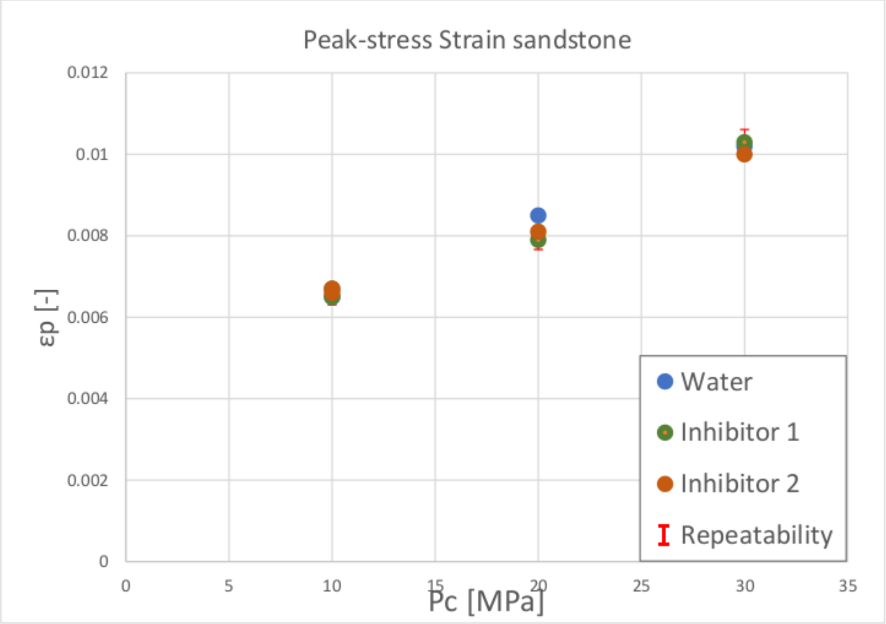

Figure 12: The figure shows the value for ϵ_p plotted against the confining pressure. At a higher confining pressure ϵ_p increases, but this value does not appear to be influenced by the difference in pore fluids. Note that the error bar is only plotted around the inhibitor 1 values. This is done solely to keep the image clear and readable.

The Mohr-Coulomb failure criteria are constructed with the obtained values for C_i and P_c (Figures 13-15) The corresponding values for S_0 are 20 ± 3, 18 ± 3 and 19 ± 3 MPa respectively. From these results it is clear that the exposure to inhibitor 1 or inhibitor 2 compared to exposure water, had no discernible effect on the mechanical rock parameters such as rock strength, angle of friction and cohesion for these sandstone samples. In addition the pH value of the solutions was measured before and after the overnight saturation period, and no changes were recorded using measurement strips with a resolution of ± 0.5.

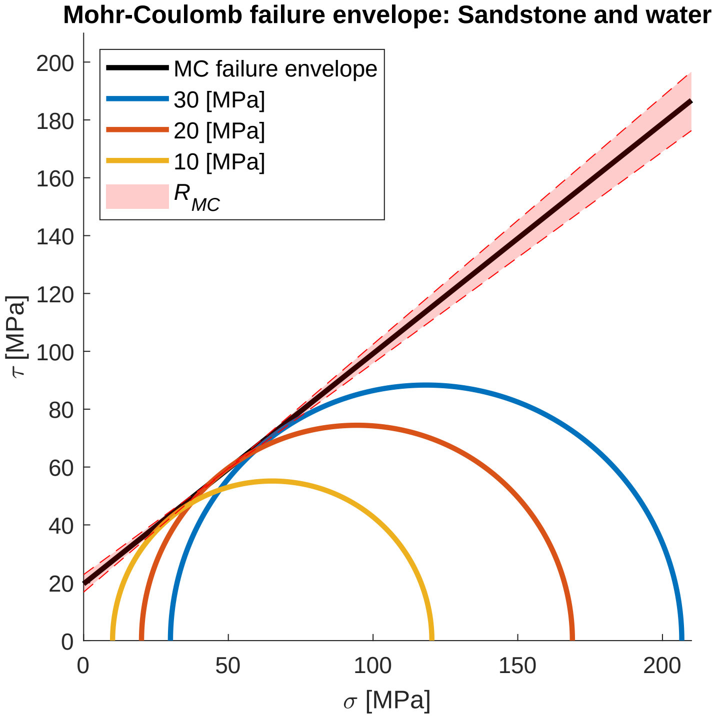

Figure 13: Graphical representation of the Mohr-Coulomb failure criterion for the sandstone set that was saturated with water.

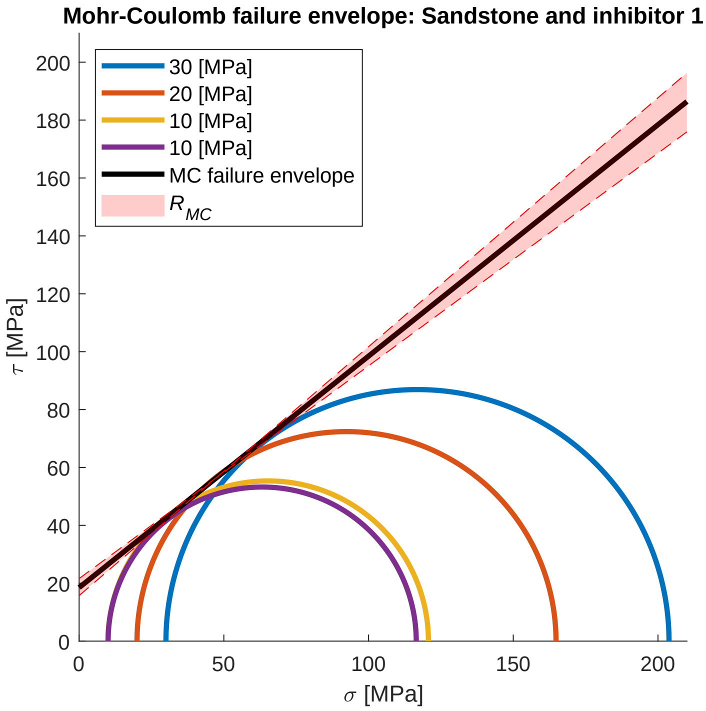

Figure 14: Graphical representation of the Mohr-Coulomb failure criterion for the sandstone set that was saturated with inhibitor 1.

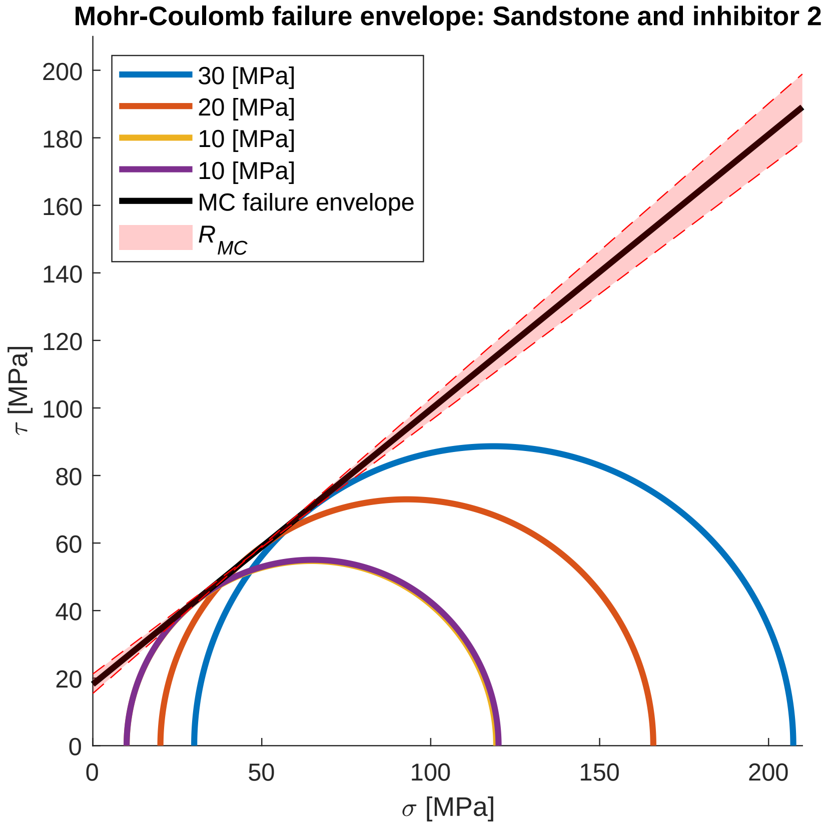

Figure 15: Graphical representation of the Mohr-Coulomb failure criterion for the sandstone set that was saturated with inhibitor 2.

4.2 Limestone

An overview of the mechanical rock properties is given in table 3. The triaxial compressive tests performed on the limestones show a difference in rock strength depending on the pore fluid as shown in figure 16. This figure represents the loading phase of the experiment. The batch of rocks which was saturated with inhibitor 1 shows a greater strength value than the samples saturated with water. The samples that were saturated with inhibitor 2 show a greater rock strength for $P_c \geq 20$ MPa. At a lower confining pressure of P_c =10 MPa the limestones exposed to inhibitor 2 show a lower differential rock strength in comparison to the batch exposed to water. The highest values for C_{30} and C_{20} are 242 MPa and 206 MPa respectively. Both values are observed for the samples which are saturated with inhibitor 2. The highest value for C_{10} (191 MPa) is observed in a sample that was saturated with inhibitor 1. Based on the repeat experiments performed at a confining pressure of 10 MPa, the limestones have a $R_C = 4$ MPa, which equates to an $r_C = 3\%$. The values for the sandstone Young's modulus range from 39 to 53 GPa. Based on the repeat experiments the r_E equals 14 %. This is illustrated in figure 17. From this image we can conclude that there is no relationship between the confining pressure and the value for E. Additionally the Young's modulus of the limestone does not appear to be affected significantly by the different fluid types. For the limestone samples the value for ϵ_p range from 0.0035 to 0.0074 (see figure 18). It seems that these values increase with an increase in confining pressure. The water-saturated samples show the lowest values for ϵ_p. However it should be noted that the repeat experiments show a relatively large R_{ϵ_p} of 0.0012, which equates to r_{ϵ_p} of 29%. Because of this large variability the previous observation could be coincidental.

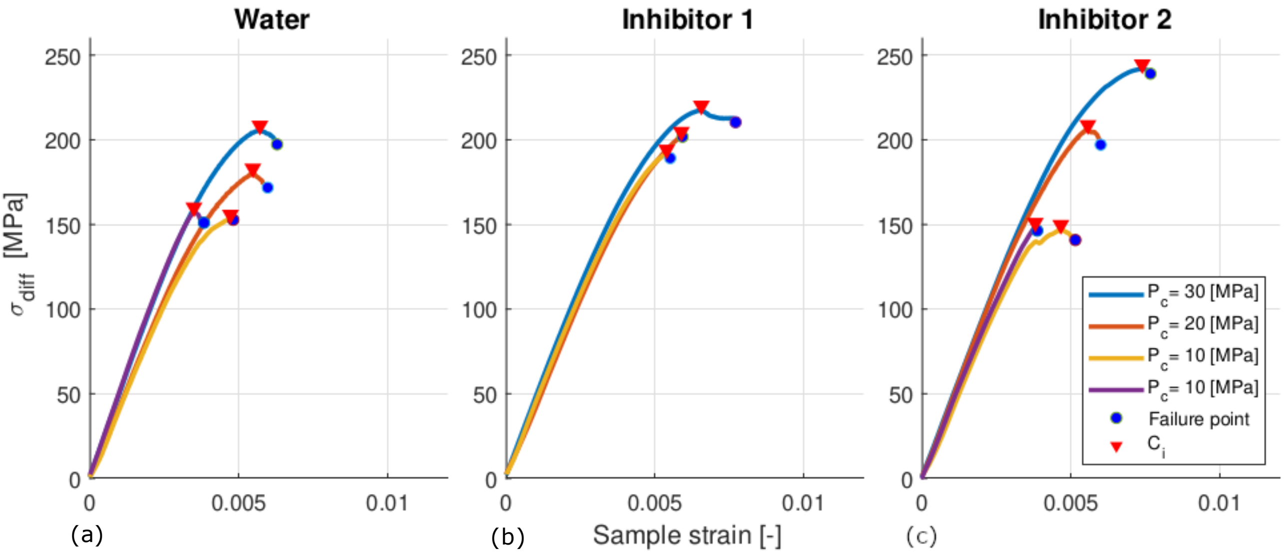

Figure 16: Differential stress-strain curves for the triaxial compressive tests performed on limestone saturated with (a) water, (b) inhibitor 1 and (c) inhibitor 2. The *failure point* marks the location where the axially supported load on the sample was rapidly declining. This was where the loading process was stopped and unloading began. The C_i markers indicate the peak axial stresses.

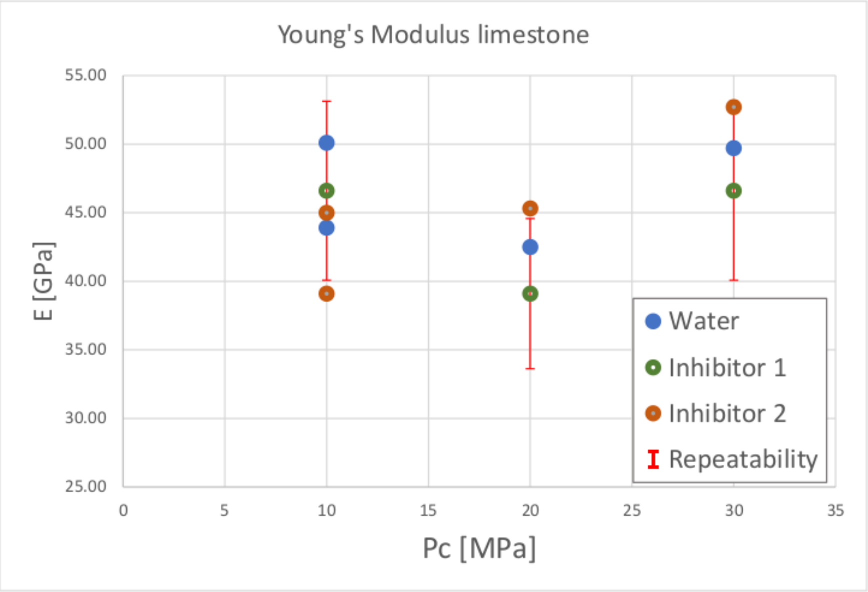

Figure 17: The limestone Young's Modulus is plotted against the confining pressure. The experiment repeatability is shown as an error bar. Note that the error bar is only plotted around the inhibitor 1 values. This is done solely to keep the image clear and readable. From the experiment results no relation between pore fluid and the Young's Modulus was established.

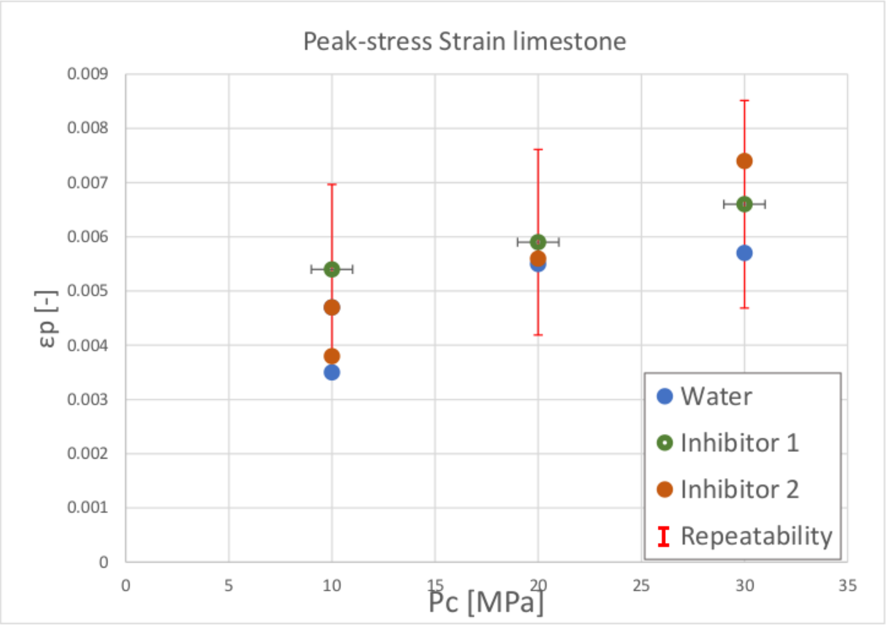

Figure 18: The figure shows the value for ϵ_p plotted against the confining pressure. At a higher confining pressure ϵ_p increases, but this value does not appear to be influenced by the difference in pore fluids. Note that the error bar is only plotted around the inhibitor 1 values. This is done solely to keep the image clear and readable.

By applying the Mohr-Coulomb failure criterion to the experimental results (Figures 19 - 21) the effect of the different fluids on the rock cohesion and the friction coefficient becomes clear: For the water saturated limestone S_0 equals 33 ± 5 MPa, for the samples saturated with inhibitor 1 S_0 is increased to 59 ± 10 MPa, whereas the samples saturated with inhibitor 2 have a reduced value for S_0 of 23 ± 3 MPa. In addition the pH values of the inhibitor solutions were measured before and after the overnight saturation period using measurement strips with a resolution of ± 0.5. Prior to testing the inhibitor 1 solution had a pH of 6.5 and the solution of inhibitor 2 had an initial pH of 5.5. After the overnight saturation period the pH value of both solutions increased to 7.0.

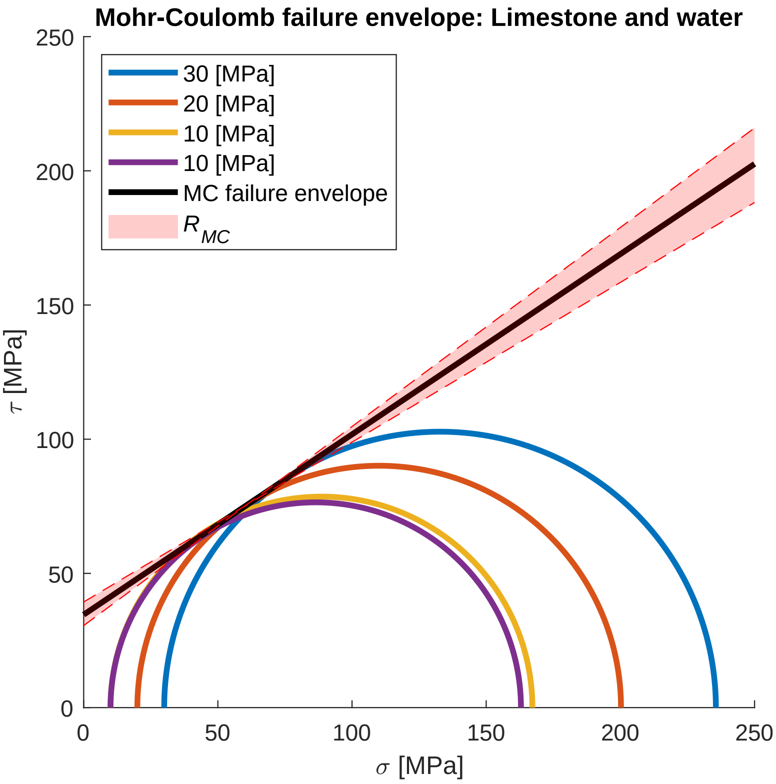

Figure 19: The Mohr-Coulomb failure criterion for the limestone set that was saturated with water.

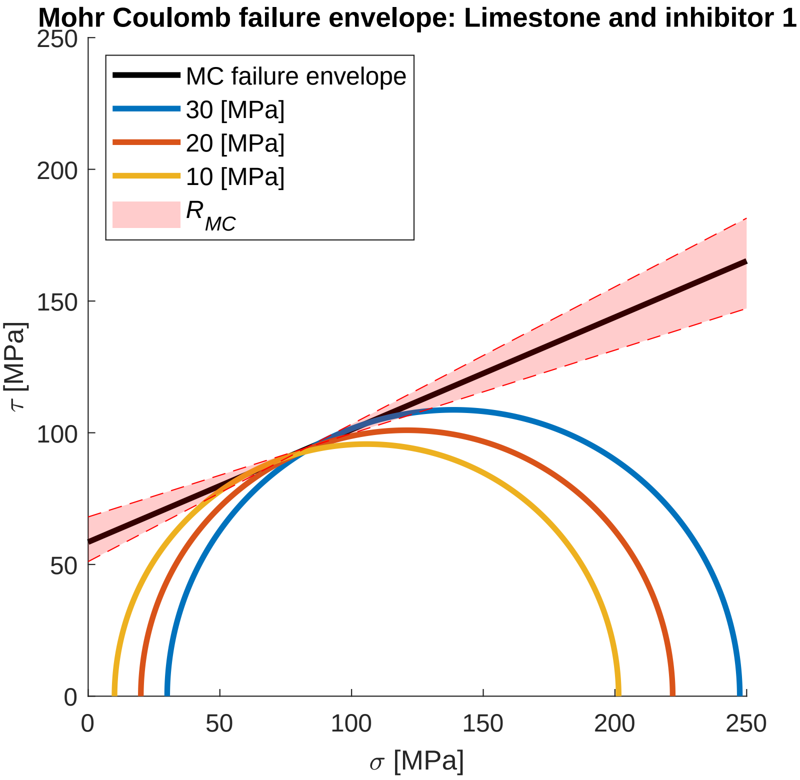

Figure 20: The Mohr-Coulomb failure criterion for the limestone set that was saturated with inhibitor 1.

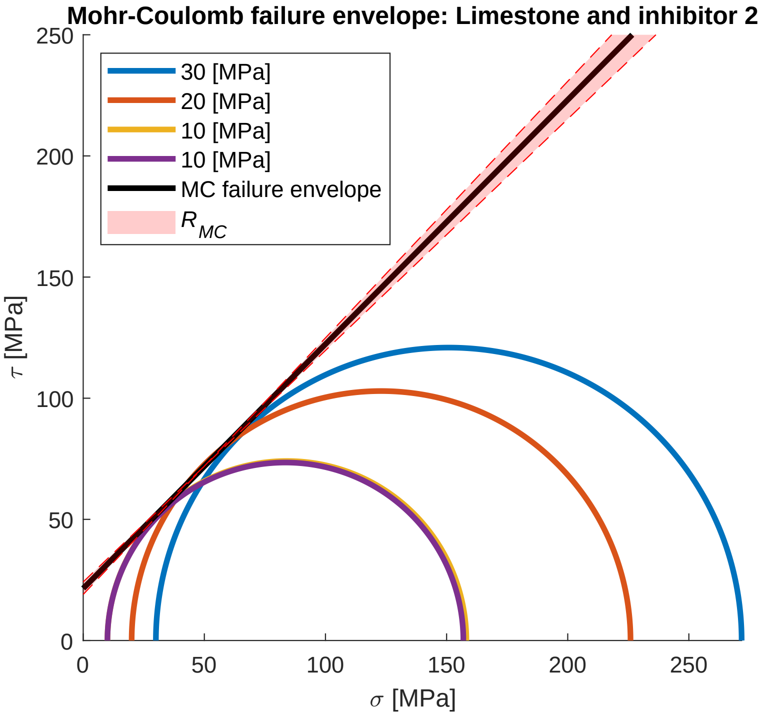

Figure 21: The Mohr-Coulomb failure criterion for the limestone set that was saturated with inhibitor 2.

4.3 Petrographic analysis

4.3.1 Micro computer tomographic images

In this section the micro-ct scans of the samples are described. One cross-sectional and a lengthwise slice are shown for each sample to complement the description. Some of the slices are annotated to highlight the fractures which might be difficult to recognize.

BS17 (full resolution)
The sandstone sample matrix consists out of grains of up to around 0.6 mm and contains intergranular porosity with several large pores up to 0.7 mm, thereby visible on these CT scans. The image looks somewhat “grainy” because of the large grains and pores. This sandstone sample shows a simple shear fracture along a single plane oblique to the axial stress. The fracture initiates at the bottom edge of the sample. It propagates at an average angle of around 40 degrees (measured from the direction of the axial compression) and crosses the entire sample. The fracture aperture is greatest towards the bottom edge and pinches out towards away from the bottom edge. The maximum aperture is measured at 0.22 mm. About half the fracture interval is readily recognized and measured, the other half has a more narrow fracture opening (aperture of 0.06 mm). Locally the fracture opening is so narrow, that it can not be observed at the current resolution. The narrow fracture aperture resulted in some residual cohesion over the failure plane.

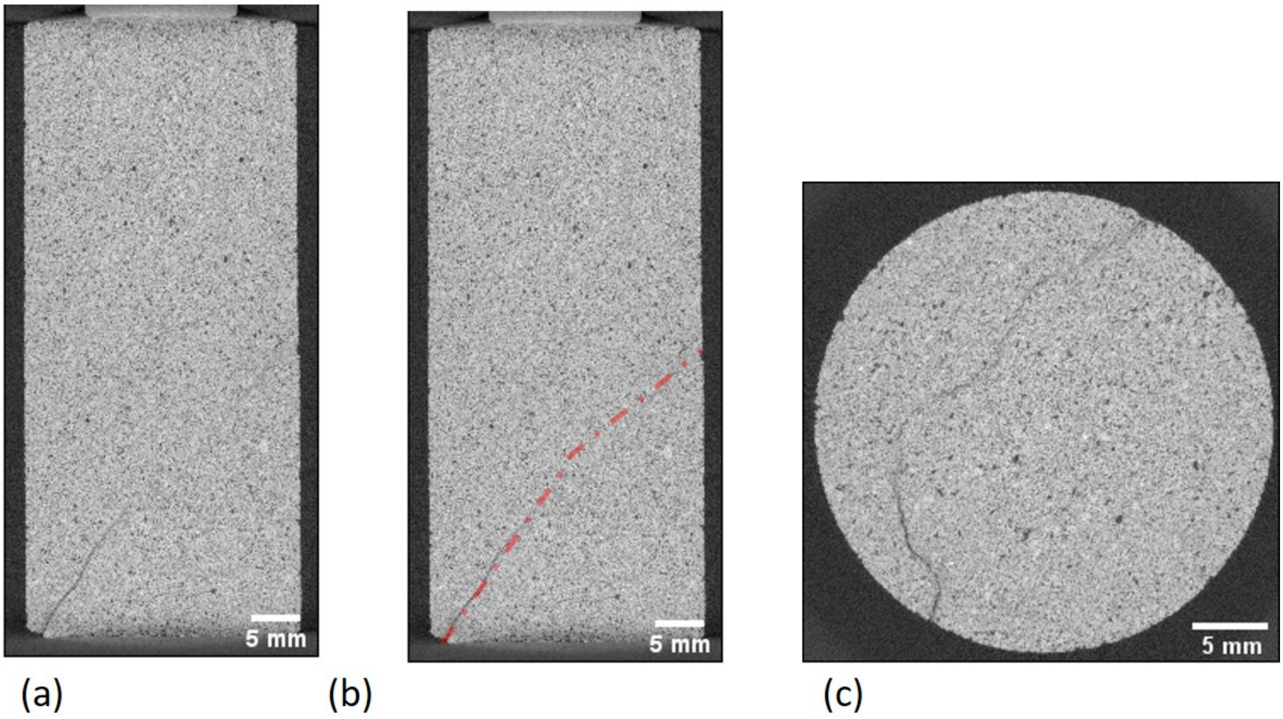

Figure 22: Micro-ct image of sample BS17. Both the horizontal and vertical slices are taken approximately from the middle of the volume. These slices were selected to give the reader clear view of the fracture pattern. (a) Lengthwise slice, (b) Annotated lengthwise slice. The dashed line is meant to help reader recognize the fracture (c) Cross-sectional slice

TM3-6 (full resolution)
This limestone sample consists out of grains which are too fine to recognize at this resolution of (28 µm)^3 per voxel. The shows a simple shear fracture along a single plane at an angle of around 30 degrees from the direction of maximum compression. The crack runs from the upper edge to the opposite outer surface of the sample. The fracture aperture is greatest towards the side-surface and pinches out towards the upper edge. The maximum opening is measured at 0.15 mm, the smallest opening can only just be distinguished at the size of one voxel (0.03 mm). The horizontal slices help make out additional fractures which are present throughout the sample, the failure planes of these fractures run parallel to the failure plane associated with the biggest fracture. These additional fractures are mostly situated within 3 mm from the main fracture. Their aperture is no greater than two voxels (0.06 mm).

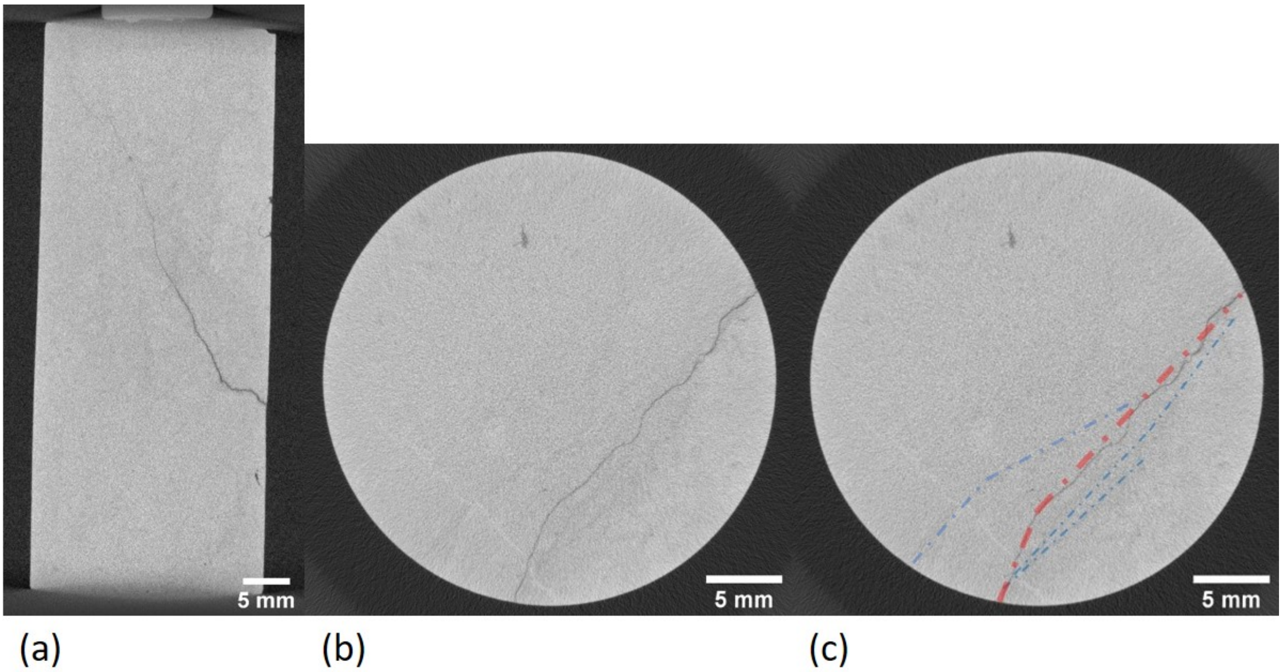

Figure 23: Micro-ct image of sample TM3-6. (a) Lengthwise slice (b) Cross-sectional slice (c) Annotated cross-sectional slice. The dashed line is meant to help reader recognize the fracture. The red line shows the fracture with the biggest aperture, the blue lines indicate the smaller fractures.

TM2-8 (full resolution)
This limestone sample consists out of grains which are too fine to recognize at this resolution of (28 µm)^3 per voxel. It has two main fractures, due to their orientation the fracture pattern can best be described as 'multiple fracturing'. One set of fractures consists of a series interlinked fractures with a similar orientation (around 30 degrees from the direction of axial compression). The fractures originate at the bottom right edge and terminate at the opposite outer surface. The aperture of these fractures is at its maximum near the outer surface, where the aperture reaches 0.12 mm. For a large interval the fracture does not exceed an aperture of more then 0.06 mm and locally the fracture becomes so narrow that it cannot be distinguished at this resolution. The plane of fracture associated with the other main fracture runs in the direction parallel to the sample axis. The other fracture originates at the bottom right edge and terminates at the top right face. The aperture is mostly 0.06 mm.

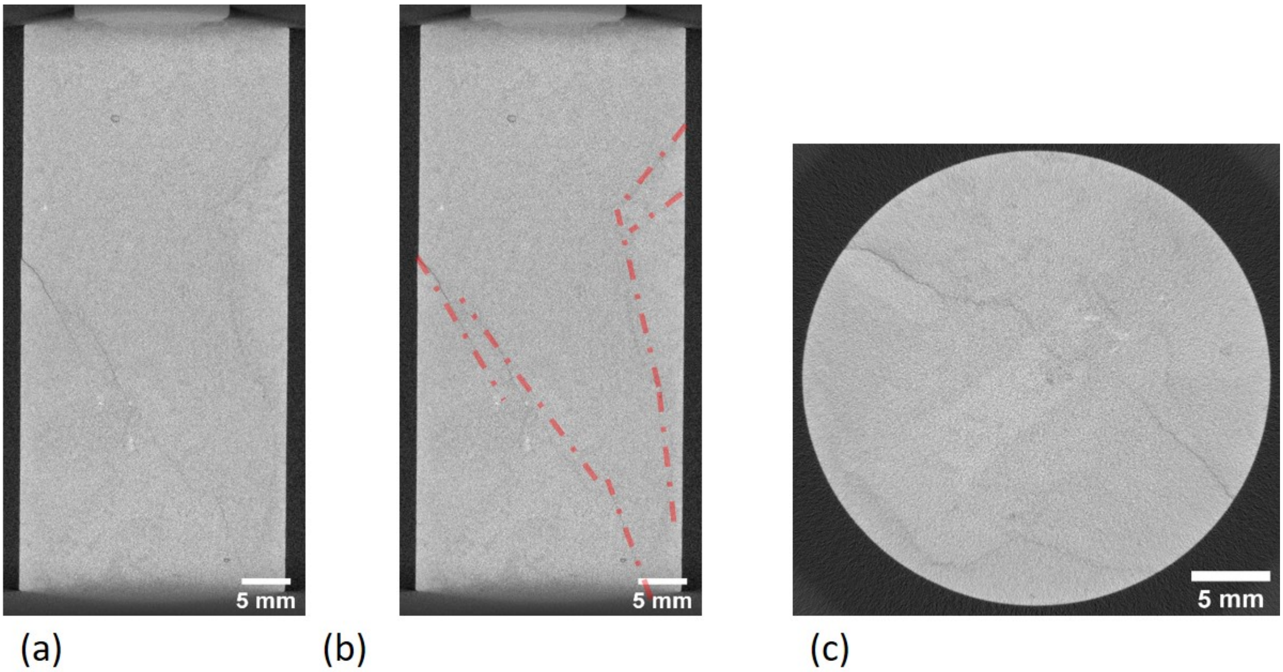

Figure 24: Micro-ct image of sample TM2-8. (a) Lengthwise slice, (b) Annotated lengthwise slice. The dashed lines are meant to help reader recognize the fractures (c) Cross-sectional slice

TM2-4 (half resolution)
This limestone sample consists out of grains which are too fine to recognize at this resolution of (56 μm)^3 per voxel. It appears to be characterized by a simple shear failure mode. A number of subparallel fractures are distinguishable, these fractures link together to form the main fracture. This main fracture originates at the bottom left edge and terminates at the opposite top right edge. It runs at an angle of around 25 degrees from the axial stress direction. The fracture aperture is 0.20 mm on average with a variance of 0.06 mm and a maximum of 0.22 mm. In addition to the main fracture, which is present throughout the entire sample, a number of thinner fractures are visible with conjugate orientations to the main fracture. The aperture of these thinner fractures barely reaches above one voxel (0.06 mm).

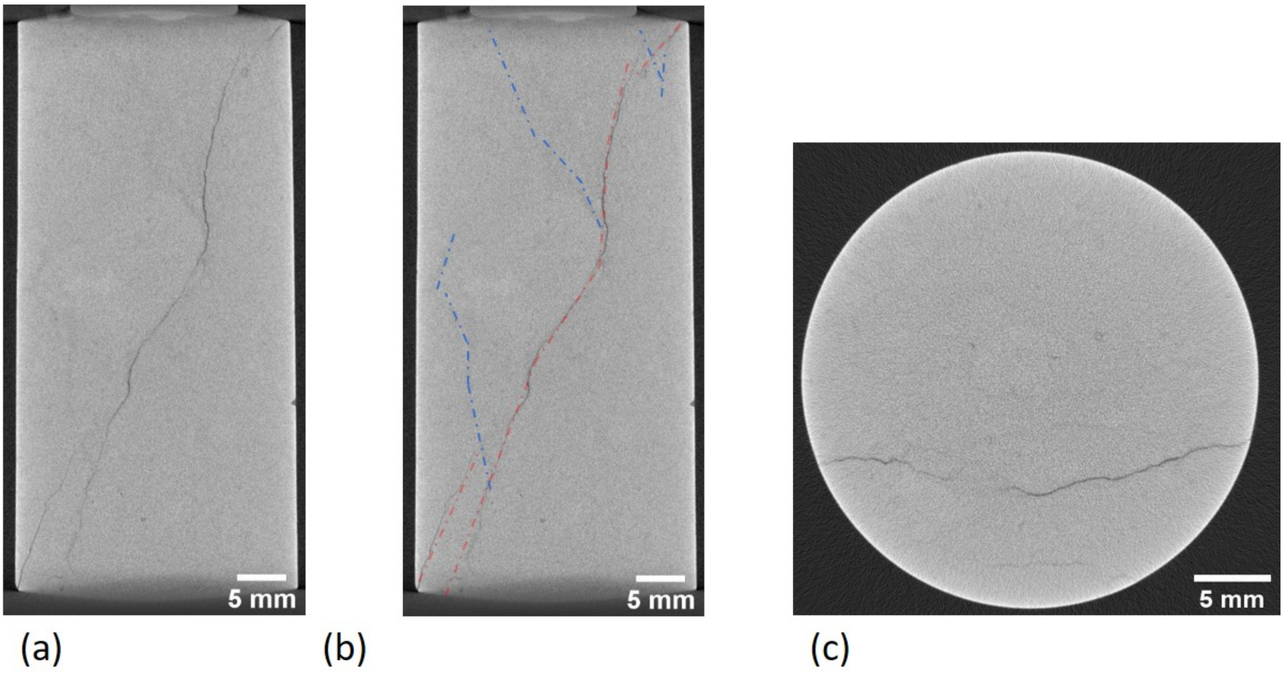

Figure 25: Micro-ct image of sample TM2-4. (a) Lengthwise slice, (b) Annotated lengthwise (c) Cross-sectional slice. The dashed lines are meant to help reader recognize the fractures. The red line indicates the fracture with the biggest aperture, the blue lines indicate the thinner fractures

TM2-5 (half resolution)
This limestone sample consists out of grains which are too fine to recognize at this resolution of (56 μm)^3 per voxel. The fracture network in this sample is classified as simple shear failure mode (according to the classification presented in figure 8). The fracture is clearly visible on the left edge of the sample, but the fracture opening narrows beyond the image resolution. The largest aperture is measured at 0.15 mm. The fracture has an angle of around 30 degrees measured from the vertical sample edge.

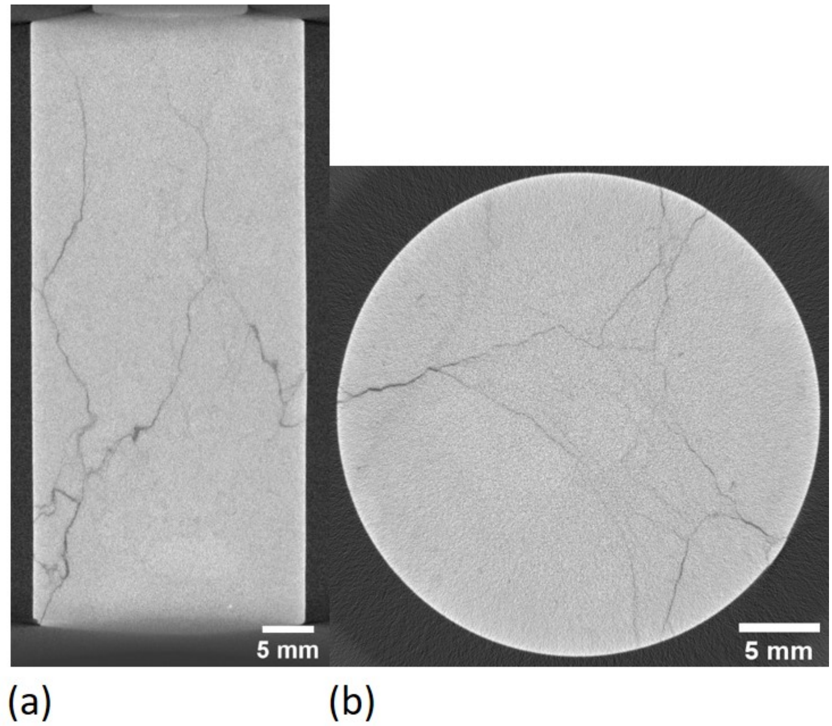

Figure 26: Micro-ct image of sample TM2-5. (a) Lengthwise slice, (b) Cross-sectional slice

TM3-1 (half resolution)
This limestone sample consists out of grains which are too fine to recognize at this resolution of (56 μm)^3 per voxel. The fracture network in this sample is classified as multiple fracturing failure mode (according to the classification presented in figure 8). The rock sample disintegrated along many planes. There is no clear orientation to this fracture network. The greatest aperture is measured at 0.22 mm over a crack that runs over almost the entire length of the sample. The other fractures have smaller openings of around 0.10 mm.

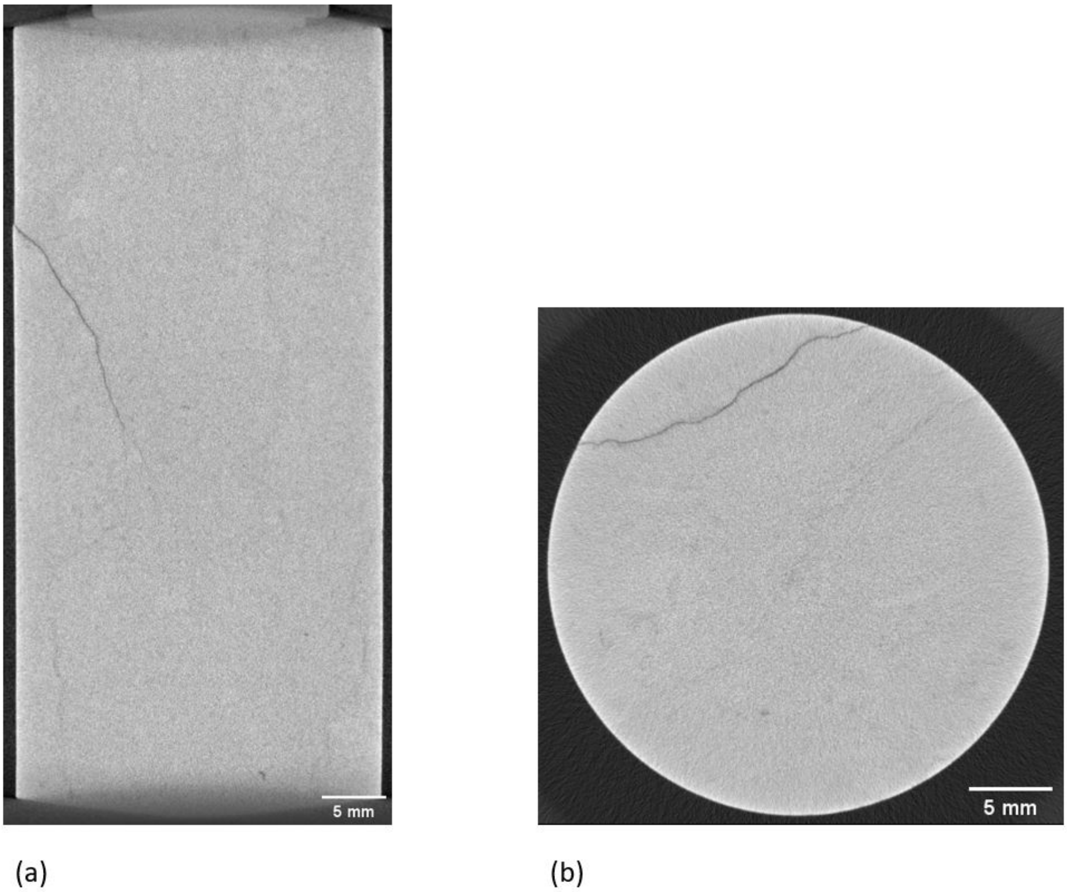

Figure 27: Micro-ct image of sample TM3-8. (a) Lengthwise slice, (b) Horizontal slice

4.3.2 Thin section analysis

BS-09

Figures 28 and 29 show the thin section of sample BS-09 under plane polarized and cross polarized light respectively. One notable feature is the fracture running diagonally across the section. It should be noted that the aperture of this fracture is not representative of the in-situ aperture, since both halves of the sample were completely split as a result of the triaxial test. The main constituent of the sample can be readily identified as monocrystalline quartz with trace amounts of opaque minerals ($< 1\%$) are visible. Based on the rock description given on the Bentheim sandstone by Peksa et al. (2015), this opaque minerals are likely hematite or goethite. The examination of the thin section reveals that the grain-size is moderately sorted and the size of most grains ranges from 0.1 mm to 0.5 mm. The grains have a subangular to subrounded shape. A damage-zone (or process-zone) is present adjacent to the fractured area. This damage-zone is characterised by a reduction in average grainsize and an increased amount of intragranular micro-cracks. These cracks are present throughout the entire thin section, but they are more prevalent in the damage-zone. The micro-cracks originate and terminate on the grain contacts. The damage zone is situated symmetrically around the fracture and has a width of roughly 2 mm to either side of the fracture.

Figure 28: Thin section image of BS-09 under polarized light

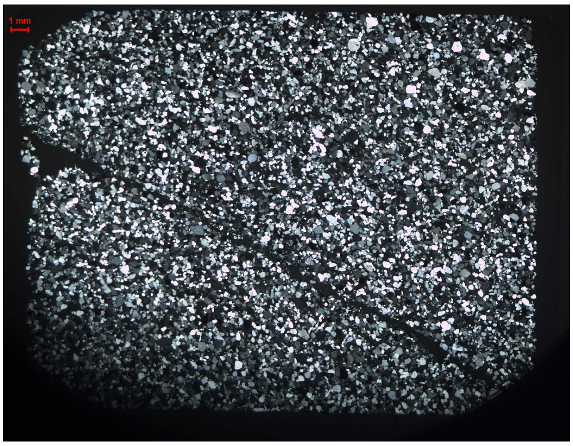

Figure 29: Thin section image of BS-09 under cross polarized light

TM2-2

Figures 30 and 31 show the thin section of sample TM2-2 under plane polarized and cross polarized light respectively. This section was saturated with inhibitor 1. The image of this thin section is notably very dark. This color can indicate a very fine grained and low-porosity material. To better visualize the thin section image for this thesis a copy of the image was modified in Adobe Photoshop CC 2018 © with a maximized brightness and an enhanced contrast (figures 32 and 33). The thin section shows a distribution of elongated thin white structures. They occur throughout the sample, but they are present most notably near the top left corner of the image. These structures are likely fossils. The crack intersects one of these structures in the top middle of the thin section, which helps to establish that there is a minimal fracture displacement as shown in figure 32. No damage zone was readily identified around the fracture. The fracture aperture varies but appears to be no greater than 0.2 mm.

Figure 30: Thin section image of TM2-2 under polarized light

Figure 31: Thin section image of TM2-2 under cross-polarized light

Figure 32: Modified thin section image of TM2-2 under polarized light with enhanced contrast and brightness. The magnification marks the very limited fracture offset.

Figure 33: Modified thin section image of TM2-2 under cross polarized light with enhanced contrast and brightness

TM4-2

Figures 34 - 37 show the thin section of sample TM4-2. This sample was saturated with demineralised water. The images 36 and 37 have been modified in Adobe Photoshop CC 2018 © to maximize brightness and to enhance the contrast. This thin section has a slightly brighter hue, compared to the image of sample TM2-2. One notable feature is the mm-scale mineral grain located in the sample of the section. In this thin section the area surrounding the fracture has a slightly darker colour. This is likely the result of a grainsize reduction within the damage-zone. This damage zone is symmetrically centered around the fracture and has a width of 1 mm to either side. On the left side of the image the fracture intersects a relatively large grain, which helps to establish that there is a minimal fracture displacement.The fracture aperture varies but apears to be no greater than 0.3 mm.

Figure 34: Thin section image of TM4-2 under polarized light

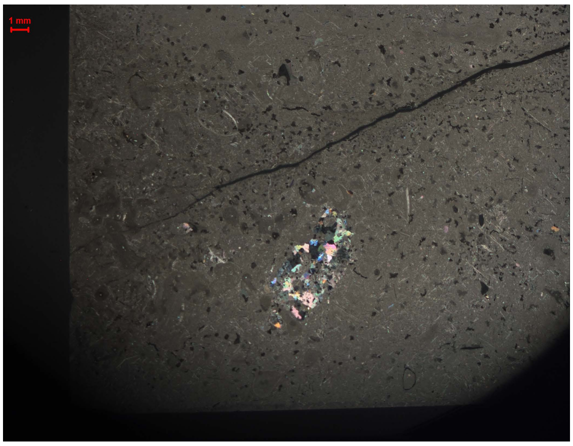

Figure 35: Thin section image of TM4-2 under polarized light

Figure 36: Modified thin section image of TM4-2 under polarized light with enhanced contrast and brightness

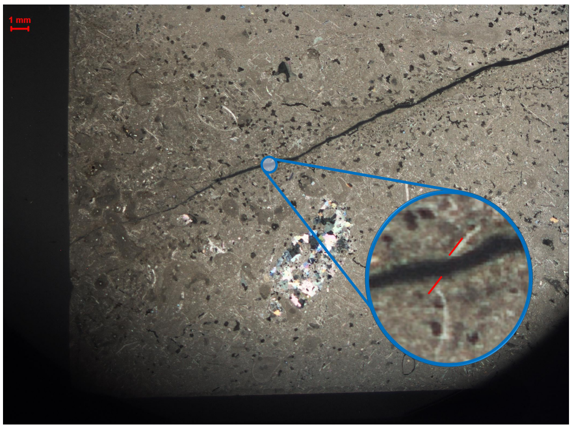

Figure 37: Modified thin section image of TM4-2 under cross polarized light with enhanced contrast and brightness. The magnification shows a fossil that is broken by the fracture. This helps with recognizing the limited fracture offset.

5 Discussion

5.1 Sandstone

The results in the previous section indicate that there is no discernible difference in the mechanical rock properties for the Bentheimer sandstone when comparing the samples that were saturated with water to the samples that were saturated with one of the inhibitors. This lack of change could be attributed to the chemical inertness of the prevalent quartz minerals in the Bentheimer sandstone. (At most environments at or near the Earth's surface quartz is considered to be chemically inert Mackenzie and Gees (1971).) The pH value of the pore fluids did not change during the overnight saturation period. This observation further strengthens the idea that no chemical rock-fluid interaction takes place. It is known from section 2.1.1 that film forming corrosion inhibitors have a nitrogen based polar head that can adsorb to a solid surface. It is described by Jada et al. (2006) that natural organic matter can adsorb on the surface of quartz particles, which leads to a modification of the surface charge. It was found that by that same paper that the adsorption kinetics are dependent on many factors such as the ionic strength, the nature of divalent cation, the pH, the adsorbent content and the temperature. We do not know for certain if any of the inhibitors are adsorbed onto the surface of the sandstone minerals in our investigation. If they did it would stand to reason that the inhibitor molecules would form a part of the electric double layer and possibly change the magnitude of the zeta potential (compared to the experiments performed with demineralised water). If ζ was affected in this manner we would expect a change in the change in the repulsive forces of the similarly charged mineral particles, and so we would expect to see a change in the mechanical rock properties. Since we did not observe any change in the mechanical rock properties for the sandstone samples, it seems unlikely that the inhibitors significantly impacted the sandstone ζ value. However it should also be noted that a study performed by Seto et al. (1997) on the influence of the zeta potential on sandstone rock strength found no significant effect on the compressive rock strength as the zeta potential changed. So from this we could conclude that even if the inhibitors affected ζ, this would not show in the results of our compressive triaxial test. However the same study did show that the tensile rock strength was strongly influenced by the zeta potential at the rock-liquid interface. Since no tensile strength experiments were conducted for this master thesis the influence of the inhibitors on the zeta potential remain uncertain.

5.2 Limestone

For the limestone experiments inhibitor 1 increased rock strength at all confining pressures. In the Mohr-Coulomb failure criterion this resulted in an increase in cohesion S_0 and a slight decrease in the coefficient of friction μ. Inhibitor 2 decreased rock strength at $P_c = 10$ MPa, and increased rock strength measured at confining pressures of 20 and 30 MPa. This is reflected in the failure criterion by a decrease in S_0 and an increase in μ. All our samples fell within a narrow range of 2.5% porosity and within this range samples did not exhibit any trends with porosity. The experiment repeatability for the rock strength was within 5 MPa for all tests, i.e. 3% of the rock strength. The only property that showed a poor repeatability was the sample strain. This value varied within 0.0012 [-] i.e. 24% for the repeat experiments. The porosity of the samples was tested prior to saturation using a pycnometer. After the overnight saturation period the a weight based porosity calculation was made. This method proved to be rather inaccurate for the reasons listed in section 3.5.1. Because of this it was not possible to accurately compare any potential change in porosity. During the saturation process the pH value increased slightly for both inhibitors which implies that some carbonate is dissolved. Prior to testing the inhibitor 1 solution had a pH of 6.5 and the solution of inhibitor 2 had an initial pH of 5.5. After the overnight saturation period the pH value of both solutions increased to 7.0. It is known from various authors that calcium carbonate can dissolve in aqueous solutions as shown in reaction R6 (e.g. Eriksson et al. (2007)).

$$\mathrm{CaCO_3(S)} \equiv \mathrm{Ca^{2+}(aq)} + \mathrm{CO_3^{2-}(aq)} \tag{R6}$$

The petrographic analysis (sections 3.4.1 and 3.4.2) show that the fracture openings and offsets are very similar across the samples saturated with different pore fluids. However the damage zone around the fracture which could be readily identified in the thin section of sample TM4-2 (water) (figures 34 - 37) was notably absent from the thin section of sample TM2-2 (inhibitor 1). Since both thin sections were tested under same confining pressure (of 20 MPa) this difference could potentially be attributed to the difference in pore fluid. We propose that the damage zone (which is only visible in TM4-2) originates from the axial sample strain that occurred between C_{20} and the failure point as shown in figure 16. The lack of sample strain after TM2-2 reached C_{20} is the reason why this damage zone around the fracture is absent from this sample. This can potentially be explained by the assumption that exposure to inhibitor 1 has increased the limestone rock strength. Which in turn could elicit more brittle deformation behaviour. Alternatively the "post-peak" sample strain could be purely incidental. In this case it would be explained by the heterogeneous nature of the rock samples. A similar difference in ϵ_p and the maximum value for ϵ can be seen in sample TM2-4 whereas this difference is notably smaller for TM4-1. These last two examples are the water saturated experiments which were tested under $P_c = 10$.

Now we want to consider the factors that could have altered the rock strength due to rock fluid interactions. Four factors will be discussed here: Calcite dissolution, crack tip blunting, changing zeta potential and grain contact lubrication. According to Alroudhan et al. (2016) an increase in acidity yields an increase in Ca^{2+} concentration. As there is a difference in initial solution acidity it follows that there is also a difference in the amount of carbonate that is dissolved. Since the solution of inhibitor 2 has a slightly higher acidity, most carbonate dissolution has likely taken place for the associated samples. Multiple authors such as Hoshino (1974), Kelsall et al. (1986) and Přikryl (2001) note that there is a inverse relationship between rock strength and porosity. This makes intuitive sense since a higher porosity means that there is less rock material to support applied load, effectively increasing the force on the individual rock particles. However we did not observe a decrease in rock strength but most limestone rocks show an increase in rock strength. This suggests that there are other factors besides calcite dissolution which influence the rock strength. One possible explanation is proposed by Rostom et al. (2013). That research suggests that calcite dissolution could cause crack tip blunting and this could have a strengthening effect on the fracture as fracture propagation is inhibited. It should be noted that this research was referring to low velocity cracks and subcritical crack propagation so the results may not be directly applicable to this thesis. Another possible controlling factor on the rock strength is the zeta potential at the rock-liquid interface. From section 2.3 it is known that the magnitude of the zeta potential considered an indication for the degree of electrostatic repulsion between similarly charged particles. In addition we know that the film forming corrosion inhibitor adsorbs to the solid surface. It is likely that this interaction impacts the electric double layer of the rock fluid interface. If the magnitude of ζ is altered because of this interaction it would likely change the repulsive forces between the limestone rock particles. A similar hypothesis is suggested by Megawati et al. (2013) based on a study on the influence of surface charge on the mechanical behaviour of high porosity chalk. These repulsive forces could affect the rock cohesion as well as the angle of internal friction. The final rock fluid interaction that will be discussed in this section is the possibility of some form a grain contact lubrication. It is known that the film forming inhibitor adsorbs to the solid surface. It could be possible that the grains on which the film is formed experience some sort of lubricating effect as a result. This could in turn alter the friction coefficient between the grain contacts. It is known from Guo and Su (2007) that the inter-particle friction affects the shear resistance of granular materials.

When considering the petrographic analysis it is difficult to draw any definitive conclusions. Given the width of the damage zone in sample TM4-2, compared to sample TM2-2 (see section 4.2 and compare figure 34 to figure 30), we interpret that the damage zone around the fracture in TM2-2 could be a shear band caused by ductile deformation. TM4-2 is a more classical example of brittle deformation. This is also in accordance with their stress-strain behaviour, as shown in figure 16. There can we see that TM4-2 shows notably more strain prior to fracturing. However as noted earlier, the sample strain showed poor repeatability in the repeat experiments. So due to the limited number of thin sections no hard conclusions should be drawn based on these results.

Based on the discussion above We propose that an increase in the magnitude of the zeta potential leads to an increase of repulsive forces which in turn lowers rock cohesion. The opposite is true when the magnitude of the zeta potential is lowered. This implies that inhibitor 1 has decreased the magnitude of ζ and inhibitor 2 has increased the magnitude of ζ. Additionally we suggest that intergranular lubrication caused by the adsorption of the inhibitor molecules on the solid surface could alter the friction coefficient between granular contacts. Since any substantial amount of calcite dissolution would lead to a decrease in rock strength, we assume that this process only plays a limited role in our experiments. The process of crack tip blunting is mainly observed in a context of subcritical crack growth, for that reason we assume that the influence of this process on our results is limited.

5.3 Limitations and recommendations

The limitations of the experiments conducted on the sandstone and limestone samples described in this thesis are listed below. They are coupled together since almost all limitations are relevant for both rock types. After each item a corresponding recommendation is suggested.

- Porosity measurements based on weight after fluid saturation were too inaccurate to determine the porosity change. The porosity of the rock was only measured with the pycnometer prior to the fluid saturation. It would have been useful to perform pycnometer porosity measurements on samples after they had been saturated with the different fluid types. This way any potential differences in porosity could be directly compared from the same type of measurement. To measure the sample porosity with the pycnometer the sample would have to be dried after the overnight saturation phase.

- The pH value was measured using indicator strips with a resolution of 0.5. Using digital pH meter would have resulted in a more accurate and precise measurement.
- The zeta potential may affect the mechanical rock properties but no direct zeta potential measurements were conducted. Performing zeta potential measurements (as done in the study by Bassioni and Taha Taqvi (2015)) would have provided direct evidence of any possible influence of the inhibitors on the zeta potential.
- No tensile strength experiments were conducted. As mentioned in the previous paragraph, Seto et al. (1997) found that the chemical alteration of the zeta potential influenced the tensile strength but not the compressive strength. It would have been useful to include a tensile strength test in the series of experiments. This would have provided an indirect method to confirm whether the zeta potential was influenced by the inhibitors.
- The triaxial tests were performed at a limited number of confining pressures, at these confining pressures the Mohr-Coulomb failure criterion is shown to be a good fit. However it is very possible that other failure criteria (such as the Hoek-Brown criterion as described by Hoek and Brown (1980)) have an overall better fit outside the tested ranges. For that reason it would be worth performing the triaxial test at additional confining pressures as well. It is mentioned by van de Watering and van der Veld (2019) that geothermal reservoirs in the Netherlands are at a depth of 1.5 to 3 km. In his master theses Mechelse (2017) suggests the horizontal pressure at 3 km depth can reach over 40 MPa. So we would recommend to at least include tests with a confining pressure of 40 MPa.
- We know that temperature is a controlling factor on: Zeta potential (section: 2.3), rock deformation behaviour (section 2.2), rate of most chemical reactions (according to Arrhenius law e.g. Connors (1990)) and finally we know that carbonate solubility decreases with an increase in temperature (e.g. Coto et al. (2012)). Our current experiments were only conducted at room temperature. So it is difficult to predict how our observations may differ from rock fluid interactions taking place at reservoir conditions. To that end it would be useful to conduct (some) experiments at the increased temperatures found in geothermal reservoirs. Production fluid temperatures are 60 -100 ° C in the Netherlands (van de Watering and van der Veld (2019)).
- For this thesis only three thin section samples were made, only two of which were sections of limestone. We discussed in the previous section that this limited number of sections, makes it difficult to determine whether observed differences (i.e. the presence of the damage zone around the fracture in sample TM4-2) are a result of sample variability or of the rock fluid interaction. To counter this uncertainty it would be useful to create thin sections from more samples. For instance it would be useful to have thin sections from experiments TM4-1, TM2-4, TM2-7 and TM3-1 which where all conducted at $P_c = 10$ MPa. In these tests the repeat experiments show a large range in the values for ϵ_1.
- During the calibration process an attempt was made to use the fluid volume displaced by the ISCO pump to calculate the radial strain. This method proved to be too inaccurate to yield consistent data. As such only the Young's modulus, and none of the other elastic moduli (e.g. Poisson's ratio, bulk modulus and shear modulus) could be calculated. Applying radial strain gauge directly to the sample would have enabled these calculations.
- The effects of the exposure time and the inhibitor concentration have not been considered during these experiments. All samples were subjected to a overnight exposure to the fluid prior to testing. To investigate the effects of the exposure duration we would suggest to perform multiple sets of experiments with both an increased (exposure periods of several weeks or months) and decreased time (minimal exposure time i.e. performing the triaxial test immediately after sample saturation).
- The effects of the inhibitor concentration in the solution on the mechanical rock properties have not been tested for this thesis. To investigate how the concentration of inhibitor fluid affects the mechanical rock properties, we would recommend to perform the triaxial tests at varying doses of inhibitor fluid. The influence of a lower dose of inhibitor fluid (in the order of several p.p.m.) would help to establish the effects of the risks of inhibitor fluid leaking into the reservoir.
- In this thesis the effects of the corrosion inhibitors on reservoir rock are compared to the effects of demineralised water. However demineralised water is not likely to naturally occur in the subsurface. Subsurface fluids have a significant amount of dissolved solids (81 - 240 g/L) (van de Watering and van der Veld (2019)). A better comparison to study the effects of the inhibitor solution on rock strength would be to use subsurface fluids instead of demineralised water in all the steps of the experiment described in this thesis.
- Currently we have only speculated that the inhibitor could alter the friction coefficient at the grain contacts. We would recommend to test this separately to verify if the inhibitor effects friction at the grain contacts. One potential way to test this separately, is to perform triaxial tests on samples that have been cut beforehand. In a set-up similar to the one used by Giorgetti et al. (2019).

- The attempt to analyse the micro CT scans in a quantitative manner did not yield any conclusive results. This was due to the limitations described in appendix B. To counter the shortcomings of this method the CT scans could be interpreted using computer algorithms to perform image segmentation as described by Vicente et al. (2017a). This could yield more conclusive data that may be better suited for interpretation.

5.4 Implications

The impact of the inhibitors on the compressive rock strength is outlined in the previous sections. In this section the implications of these findings on the geothermal production process are discussed. One important note prior to this discussion is that under normal operating procedure inhibitor products are continuously dosed in the production well just above the reservoir level van de Watering and van der Veld (2019). So the inhibitor solution should not enter the reservoir rock but rather enters the production well tube together with the production fluids. It is unlikely that any substantial amounts of inhibitor fluids come into contact with the reservoir rock. However there are imaginable scenarios where unintentional reservoir rock exposure could occur. For instance if the production is disrupted whilst the inhibitor injection continues. Additionally as stated in section 2.1.1 in a hazard and operability analysis performed by van de Watering and van der Veld (2019) it was concluded that there is a risk of leakage of inhibitor solution into the geothermal reservoir. From the findings in this thesis such a scenario would only affect rock strength if the affected reservoir rock is a limestone. Furthermore the rock strength would only be negatively impacted under certain conditions: At the tested confining pressures our limestone rock showed an increase in rock strength when it was saturated with inhibitor 1. If we use the Mohr-Coulomb failure criterion to predict the rock strength outside the tested ranges we expect that the limestone rock (saturated with inhibitor 1) will show a decrease in rock strength due to the decreased coefficient of friction. By contrast limestone rock exposed to inhibitor 2 is shown to have a lower rock strength only at low confining pressures. Although this rock strength reduction will not likely cause the immediate failure of the rock, for the subsurface pressures normally encountered in geothermal production from sedimentary rocks.

6 Conclusion

The goal of this thesis was to experimentally investigate whether mechanical rock properties are affected by exposure to corrosion inhibitors that are commonly used in a geothermal production setting. This was done by performing triaxial compressive tests on rock samples that were saturated with inhibitor solutions. The following conclusions can be drawn:

1. Sandstone exposure to the different inhibitors had no effect on: $(\sigma_{diff})_{max}$, ϵ, E, S_o and μ. This is likely due to the inert nature of the quartz grains. Other research has shown that tensile rock strength of sandstones can be influenced by a change in zeta potential. However in this research no tensile experiments were conducted. Besides there are many factors that dictate the quartz adsorption kinetics and for this research we are uncertain whether any inhibitor molecules actually adsorbed on the quartz particle surfaces. The influence of the zeta potential would require separate testing.
2. Limestone exposure to the first corrosion inhibitor led to: an increase in $(\sigma_{diff})_{max}$ and S_o. On the other hand the values for ϵ and E appear to be unaffected. Finally the value of μ is decreased. Overall inhibitor 1 has a strengthening effect on limestone at the tested confining pressures.A number of potential controlling mechanisms are proposed:
   - A change in zeta potential may lead to a decrease in the electrostatic repulsive forces at the grain contacts. This could lead to an increase in rock cohesion.
   - The adsorption of the inhibitor molecules may alter the friction coefficient at the grain contacts.
3. Limestone exposure to the second corrosion inhibitor led to: an increase in $(\sigma_{diff})_{max}$ at higher confining pressures (20 and 30 MPa) and an increase in μ. Again the values for ϵ and E appear to be unaffected. The values for S_o and the $(\sigma_{diff})_{max}$ at a low confining pressure (10 MPa) decreased. The proposed mechanisms involved in these changes are:
   - A change in zeta potential may lead to a increase in the electrostatic repulsive forces at the grain contacts. This could lead to the decrease in rock cohesion.
   - The adsorption of the inhibitor molecules may alter the friction coefficient at the grain contacts.

   The interaction between the limestone and the inhibitor fluid is not fully understood. And the previously proposed mechanisms should still be investigated separately. From the results in this report it can be concluded that the reservoir rock should not be negatively impacted by exposure to the tested inhibitors at prevalent subsurface pressures.

7 Bibliography

References

A Alroudhan, J Vinogradov, and MD Jackson. Zeta potential of intact natural limestone: Impact of potential-determining ions ca, mg and so4. *Colloids and Surfaces A: Physicochemical and Engineering Aspects*, 493: 83–98, 2016.

analytik.co.uk. Zeta potential – what is it and how can it be characterised?, sep 2020. URL `https://analytik.co.uk/zeta-potential-what-is-it-and-how-can-it-be-characterised/`.

Ghada Bassioni and Syed Taha Taqvi. Wettability studies using zeta potential measurements. *Journal of Chemistry*, 2015, 2015.

A Basu, DA Mishra, and K Roychowdhury. Rock failure modes under uniaxial compression, brazilian, and point load tests. *Bulletin of Engineering Geology and the environment*, 72(3-4):457–475, 2013.

Hoss Belyadi, Ebrahim Fathi, and Fatemeh Belyadi. *Hydraulic fracturing in unconventional reservoirs: theories, operations, and economic analysis*. Gulf Professional Publishing, 2019.

H.A. Boogaert and Wim Kouwe. Stratigraphic nomenclature of the netherlands, revision and update by rgd and nogepa. *Mededelingen Rijks Geologische Dienst*, 50:1–40, 01 1993.

Sayantan Chakraborty, Rohan Bisai, Sathish Kumar Palaniappan, and Samir Kumar Pal. Failure modes of rocks under uniaxial compression tests: An experimental approach. *Journal of Advances in Geotechnical Engineering*, 2(3), 2019.

K.A. Connors. *Chemical Kinetics: The Study of Reaction Rates in Solution*. VCH, 1990. ISBN 9781560810063. URL `https://books.google.nl/books?id=nHux3YED1HsC`.

Baudilio Coto, C Martos, José L Peña, Rosalía Rodríguez, and Gabriel Pastor. Effects in the solubility of caco3: Experimental study and model description. *Fluid Phase Equilibria*, 324:1–7, 2012.

Elsemiek Croese. Microbiology in geothermal operations. *Kennisagenda aardwarmte*, 2018. URL `https://www.kasalsenergiebron.nl/content/user_upload/Final_Report_Microorganisms_in_geothermal_operations_20177513_1987.pdf`.

Merriam-Webster Dictionary. the merriam-webster dictionary, 2020. URL `https://www.merriam-webster.com/dictionary/inhibitor`.

C. Dubelaar and Timo G. Nijland. The bentheim sandstone: Geology, petrophysics, varieties and its use as dimension stone. In Giorgio Lollino, Daniele Giordan, Cristian Marunteanu, Basiles Christaras, Iwasaki Yoshinori, and Claudio Margottini, editors, *Engineering Geology for Society and Territory - Volume 8*, pages 557–563, Cham, 2015. Springer International Publishing. ISBN 978-3-319-09408-3.

Rasmus Eriksson, Juha Merta, and Jarl B Rosenholm. The calcite/water interface: I. surface charge in indifferent electrolyte media and the influence of low-molecular-weight polyelectrolyte. *Journal of colloid and interface science*, 313(1):184–193, 2007.

OSI Fayomi, IG Akande, and S Odigie. Economic impact of corrosion in oil sectors and prevention: An overview. In *Journal of Physics: Conference Series*, volume 1378, page 022037. IOP Publishing, 2019.

H. Fossen. *Structural Geology*. Cambridge University Press, 2010. ISBN 9781139488617. URL `https://books.google.nl/books?id=01PI5jhjiiQC`.

Ingvar B Fridleifsson. Geothermal energy for the benefit of the people. *Renewable and sustainable energy reviews*, 5(3):299–312, 2001.

Carolina Giorgetti, Telemaco Tesei, Marco Maria Scuderi, and Cristiano Collettini. Experimental insights into fault reactivation in gouge-filled fault zones. *Journal of Geophysical Research: Solid Earth*, 124(4):4189–4204, 2019.

Peijun Guo and Xubin Su. Shear strength, interparticle locking, and dilatancy of granular materials. *Canadian Geotechnical Journal*, 44(5):579–591, 2007.

John Handin and Jr. Hager, Rex V. Experimental Deformation of Sedimentary Rocks Under Confining Pressure: Tests at Room Temperature on Dry Samples1. *AAPG Bulletin*, 41(1):1–50, 01 1957. ISSN 0149-1423. doi: 10.1306/5CEAE5FB-16BB-11D7-8645000102C1865D. URL https://doi.org/10.1306/5CEAE5FB-16BB-11D7-8645000102C1865D.

MJ Heap, P Baud, PG Meredith, AF Bell, and IG Main. Time-dependent brittle creep in darley dale sandstone. *Journal of Geophysical Research: Solid Earth*, 114(B7), 2009.

E Hilner, Martin Peter Andersson, Tue Hassenkam, Jesper Matthiesen, PA Salino, and Susan Louise Svane Stipp. The effect of ionic strength on oil adhesion in sandstone–the search for the low salinity mechanism. *Scientific reports*, 5(1):1–9, 2015.

Evert Hoek and Edwin T Brown. Empirical strength criterion for rock masses. *Journal of Geotechnical and Geoenvironmental Engineering*, 106(ASCE 15715), 1980.

K Hoshino. Effect of porosity on the strength of the clastic sedimentary rocks. In *Proceedings of the 3rd Congress of the International Society for Rock Mechanics, Denver, CO*, pages 511–516. AA Balkema, Rotterdam,, 1974.

Robert J Hunter. *Zeta potential in colloid science: principles and applications*, volume 2. Academic press, 2013.

E.H. Isaaks, D.A.E.S.E.H. Isaaks, R.M. Srivastava, and Knovel (Firm). *Applied Geostatistics*. Oxford University Press, 1989. ISBN 9780195050134. URL https://books.google.nl/books?id=vC2dcXFLI3YC.

A Jada, R Ait Akbour, and J Douch. Surface charge and adsorption from water onto quartz sand of humic acid. *Chemosphere*, 64(8):1287–1295, 2006.

John Conrad Jaeger, Neville GW Cook, and Robert Zimmerman. *Fundamentals of rock mechanics*. John Wiley & Sons, 2009.

Yuntao Ji, Stephen A. Hall, Patrick Baud, and Teng-fong Wong. Characterization of pore structure and strain localization in Majella limestone by X-ray computed tomography and digital image correlation. *Geophysical Journal International*, 200(2):701–719, 12 2014. ISSN 0956-540X. doi: 10.1093/gji/ggu414. URL https://doi.org/10.1093/gji/ggu414.

Malcolm A Kelland. *Production chemicals for the oil and gas industry*. CRC press, 2014.

Peter C Kelsall, Robert J Watters, Joseph G Franzone, et al. Engineering characterization of fissured, weathered dolerite and vesicular basalt. In *The 27th US Symposium on Rock Mechanics (USRMS)*. American Rock Mechanics Association, 1986.

Emmanuelle Klein and Thierry Reuschlé. *A Model for the Mechanical Behaviour of Bentheim Sandstone in the Brittle Regime*, pages 833–849. Birkhäuser Basel, Basel, 2003. ISBN 978-3-0348-8083-1. doi: 10.1007/978-3-0348-8083-1_3. URL https://doi.org/10.1007/978-3-0348-8083-1_3.

Roman Koch and Christian Weiss. Field trip a: basin-platform transitions in upper jurassic limestones and dolomites of the northern franconian alb (germany). *Zitteliana*, pages 43–56, 2005.

M Lingenfelder, J Fuhr, J Gayone, and H Ascolani. Encyclopedia of interfacial chemistry, 2018.

Guang Wei Lu and Ping Gao. Chapter 3 - emulsions and microemulsions for topical and transdermal drug delivery. In Vitthal S. Kulkarni, editor, *Handbook of Non-Invasive Drug Delivery Systems*, Personal Care Cosmetic Technology, pages 59 – 94. William Andrew Publishing, Boston, 2010. ISBN 978-0-8155-2025-2. doi: https://doi.org/10.1016/B978-0-8155-2025-2.10003-4. URL http://www.sciencedirect.com/science/article/pii/B9780815520252100034.

Fred T Mackenzie and Rudi Gees. Quartz: synthesis at earth-surface conditions. *Science*, 173(3996):533–535, 1971.

AJ McMahon. The mechanism of action of an oleic imidazoline based corrosion inhibitor for oilfield use. *Colloids and surfaces*, 59:187–208, 1991.

Eelco Mechelse. The in-situ stress field in the netherlands: Regional trends, local deviations and an analysis of the stress regimes in the northeast of the netherlands. 2017.

M Megawati, A Hiorth, and MV Madland. The impact of surface charge on the mechanical behavior of high-porosity chalk. *Rock mechanics and rock engineering*, 46(5):1073–1090, 2013.

Mohammad Hadi Mehranpour and Pinnaduwa HSW Kulatilake. Comparison of six major intact rock failure criteria using a particle flow approach under true-triaxial stress condition. *Geomechanics and Geophysics for Geo-Energy and Geo-Resources*, 2(4):203–229, 2016.

Eckhard Mönnig. Der jura von norddeutschland in der stratigraphischen tabelle von deutschland 2002. *Newsletters on Stratigraphy*, 41(1-3):253–261, 06 2006. doi: 10.1127/0078-0421/2005/0041-0253. URL `http://dx.doi.org/10.1127/0078-0421/2005/0041-0253`.

Ian Douglas Morrison and Sydney Ross. *Colloidal dispersions: suspensions, emulsions, and foams.* Wiley-Interscience New York, 2002.

Birgit Niebuhr and Thomas Pürner. Plattenkalk und frankendolomit ? lithostratigraphie der weißjuragruppe der frankenalb (außeralpiner oberjura, bayern). *Schriftenreihe der Deutschen Gesellschaft für Geowissenschaften*, 83:5–72, 03 2014. doi: 10.1127/sdgg/83/2014/5. URL `http://dx.doi.org/10.1127/sdgg/83/2014/5`.

MS Paterson. Experimental rock deformation——the brittle field speringer-verlag, 1978.

AE Peksa, KHAA Wolf, and PLJ Zitha. Bentheimer sandstone revisited for experimental purposes. *Marine and Petroleum Geology*, 67(November):701–719, 2015. ISSN 0264-8172. doi: 10.1016/j.marpetgeo.2015.06.001. harvest.

N. Perez. *Fracture Mechanics*. Springer International Publishing, 2016. ISBN 9783319249995. URL `https://books.google.nl/books?id=cQTWDAAAQBAJ`.

Lekan Taofeek Popoola, Alhaji Shehu Grema, Ganiyu Kayode Latinwo, Babagana Gutti, and Adebori Saheed Balogun. Corrosion problems during oil and gas production and its mitigation. *International Journal of Industrial Chemistry*, 4(1):35, 2013.

R Přikryl. Some microstructural aspects of strength variation in rocks. *International Journal of Rock Mechanics and Mining Sciences*, 38(5):671–682, 2001.

Fatma Rostom, Anja Røyne, Dag Kristian Dysthe, and François Renard. Effect of fluid salinity on subcritical crack propagation in calcite. *Tectonophysics*, 583:68–75, 2013.

EH Rutter. The effects of strain-rate changes on the strength and ductility of solenhofen limestone at low temperatures and confining pressures. In *International Journal of Rock Mechanics and Mining Sciences & Geomechanics Abstracts*, volume 9, pages 183–189. Elsevier, 1972.

Johannes Schindelin, Ignacio Arganda-Carreras, Erwin Frise, Verena Kaynig, Mark Longair, Tobias Pietzsch, Stephan Preibisch, Curtis Rueden, Stephan Saalfeld, Benjamin Schmid, et al. Fiji: an open-source platform for biological-image analysis. *Nature methods*, 9(7):676–682, 2012.

M Seto, Dilip K Nag, VS Vutukuri, and K Katsuyama. Effect of chemical additives on the strength of sandstone. *International Journal of Rock Mechanics and Mining Sciences*, 34(3-4):280–e1, 1997.

Ahmed M Shehata, Hisham A Nasr-El-Din, et al. Zeta potential measurements: Impact of salinity on sandstone minerals. In *SPE International Symposium on Oilfield Chemistry*. Society of Petroleum Engineers, 2015.

stichting DAP. About stichting dap, aug 2020. URL `https://www.stichtingdap.nl/`.

C.T. Sun and Z. Jin. *Fracture Mechanics*. Elsevier Science, 2011. ISBN 9780123850027. URL `https://books.google.nl/books?id=LfqMaqVw-jMC`.

T Szwedzicki and W Shamu. The effect of discontinuities on strength of rock samples. In *Proceedings of the Australasian Institute of Mining and Metallurgy*, volume 304, pages 23–28. Citeseer, 1999.

S Tamari. Optimum design of the constant-volume gas pycnometer for determining the volume of solid particles. *Measurement Science and Technology*, 15(3):549–558, feb 2004. doi: 10.1088/0957-0233/15/3/007. URL `https://doi.org/10.10882F0957-0233%2F15%2F3%2F007`.

Nandor Tamaskovics, Detlev Tondera, Guido Blöcher, Inga Moeck, Pavel Pavlov, Curd Bems, and Stephan Hild. Geothermal research project "algäu 2.0" research concepts, laboratory investigations and planning operations.

Engineering ToolBox. Young's modulus - tensile and yield strength for common materials, mar 2020.

Renaud Toussaint, Einat Aharonov, Daniel Koehn, J-P Gratier, Martin Ebner, Patrick Baud, Alexandra Rolland, and Francois Renard. Stylolites: A review. *Journal of Structural Geology*, 114:163–195, 2018.

M.F. Triola. *Essentials of Statistics*. Pearson Education, 2014. ISBN 9780321924636. URL `https://books.google.nl/books?id=QZN-AgAAQBAJ`.

HA Van Adrichem Boogaert and WPF Kouwe. Stratigraphic nomenclature of the netherlands, revision and update by rgd and nogepa. 1993.

Fenna van de Watering and Raphaël van der Veld. (environmental) impact of inhibitors applied in the geothermal sector in the netherlands. In *European Geothermal Congress*. Witteveen+Bos, June 2019.

M Vicente, Jesús Mínguez, and Dorys C González. *The use of computed tomography to explore the microstructure of materials in civil engineering: from rocks to concrete*. InTech, 2017a.

Miguel A. Vicente, Jesús Mínguez, and Dorys C. González. The use of computed tomography to explore the microstructure of materials in civil engineering: From rocks to concrete. In Ahmet Mesrur Halefoglu, editor, *Computed Tomography*, chapter 10. IntechOpen, Rijeka, 2017b. doi: 10.5772/intechopen.69245. URL `https://doi.org/10.5772/intechopen.69245`.

K Wolański, W Zarudzki, H Kiersnowski, M Dohnalik, K Drabik, A Urbaniec, and R Skupio. X-ray computed tomography (ct) applied for rock core analysis. *Bull. Russ. Accad. Nat. Sci*, 5:43–50, 2017.

Sheng-Qi Yang, Hong-Wen Jing, and Shan-Yong Wang. Experimental investigation on the strength, deformability, failure behavior and acoustic emission locations of red sandstone under triaxial compression. *Rock mechanics and rock engineering*, 45(4):583–606, 2012.

Mingqing You. Three independent parameters to describe conventional triaxial compressive strength of intact rocks. *Journal of Rock Mechanics and Geotechnical Engineering*, 2(4):350–356, 2010.

Shao-Long Zhong, Zhi-Min Dang, Wen-Ying Zhou, and Hui-Wu Cai. Past and future on nanodielectrics. *IET Nanodielectrics*, 1(1):41–47, 2018.

A Gas pycnometry

Gas pycnometry can be used to determine the volume of solid particles of an object of interest. This procedure relies on Boyle-Mariotte's Law (equation 13) in combination with the assumptions that are listed below, as mentioned by Tamari (2004):

1. The gas inside the pycnometer behaves ideally.
   (Its compressibility is negligible and it does not adsorb on solids.)
2. The sample and the components are rigid.
3. The pycnometer is gas-tight and the expanding gas quickly reaches a static equilibrium.

$$P_1 \cdot V_1 = P_2 \cdot V_2 \tag{13}$$

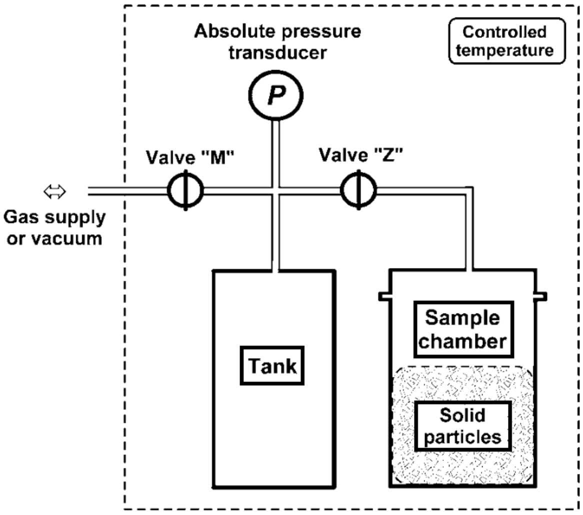

Figure 38: Diagram of a gas pycnometer modified from Tamari (2004). The sample chamber and the tank, initially filled with gas at two different pressures, are connected by opening valve "Z". The final gas pressure indicates how much of the sample-chamber volume is occupied by the solid particles.

The procedure for determining the sample porosity involved measuring the external dimensions of the sample. This gave the bulk rock volume V_b. Additionally the pycnometer was calibrated so that the volume of the tank V_t and the volume of the sample chamber V_c are known. When relating figure 38 to equation 13, the left-hand-side of the equation resembles the situation where valve "Z" is in a closed position. In this situation the volume is equal to the volume of the tank. The right-hand side of the equation represents the situation where valve "Z" is opened, so that gas can freely flow from the tank to the sample chamber. This will result in a pressure drop which is dependent on the available space within the sample chamber. Equation 13 can be rewritten to:

$$P_1 \cdot V_t = P_2 \cdot (V_t + V_c - V_p) \tag{14}$$

In the previous equation, V_m is the volume occupied by the solid particles of the rock matrix. By grouping the known terms of equation 14, this can be rewritten to:

$$V_m = V_t + V_c - \frac{P_1 \cdot V_t}{P_2} \tag{15}$$

The pore volume is the difference between the bulk rock volume and the volume occupied by the matrix particles as shown in equation 16. From the pore volume and the bulk rock volume the porosity can be calculated, as shown in equation 17.

$$V_p = V_b - V_m \tag{16}$$

$$\phi = \frac{V_p}{V_b} \tag{17}$$

B Statistical fracture aperture

In this appendix the statistical aperture method is treated. It is treated separately here because a significant amount of time was spent on performing this method, but due to the limitations listed below the author wants to emphasize that we should be very careful with the interpretation of the results. The method involved looking at equidistant horizontal slices throughout the fractured interval of the sample. These slices were spaced 5.6 mm apart (200 voxels at full resolution and 100 voxels at half resolution). In each slice the fracture aperture was measured at three separate locations as shown in figure 39. The results of these measurements are listed in the tables below. The reasons why this data should not be considered as conclusive are listed here:

- The manual apertures measurements are sensitive to researcher error and bias. (To illustrate this the aperture was for sample TM2-4 was measured a second time resulting in a different outcome as shown in figure 40
- This error is partly caused by the difficulty of interpreting data. In addition the location of the measurement strongly affects the results. The fracture aperture in adjacent voxels can already vary significantly as is shown in figure 41
- Using the method described above we obtain a very small sample size in comparison to the total amount of available data.

For the reasons listed above it was decided to focus mainly on the qualitative nature of the fractures.

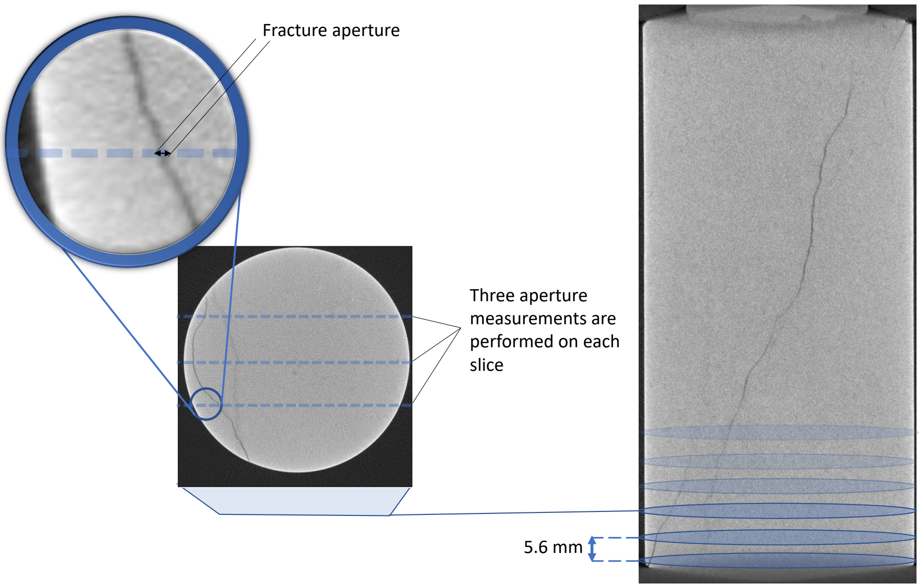

Figure 39: Aperture measurements were performed at regular intervals on equidistant horizontal slices to obtain a statistical dataset of the fracture aperture.

Summary fracture measurements					
Sample	TM2-4	TM3-6	TM2-5	TM2-8	TM3-1
Mean [mm]:	0,14	0,10	0,16	0,06	0,11
Max [mm]:	0,22	0,15	0,22	0,12	0,18
Min [mm]	0,06	0,03	0,06	0,03	0,06
Variance [mm]:	4,5E-02	1,1E-03	2,9E-03	6,5E-04	1,2E-03

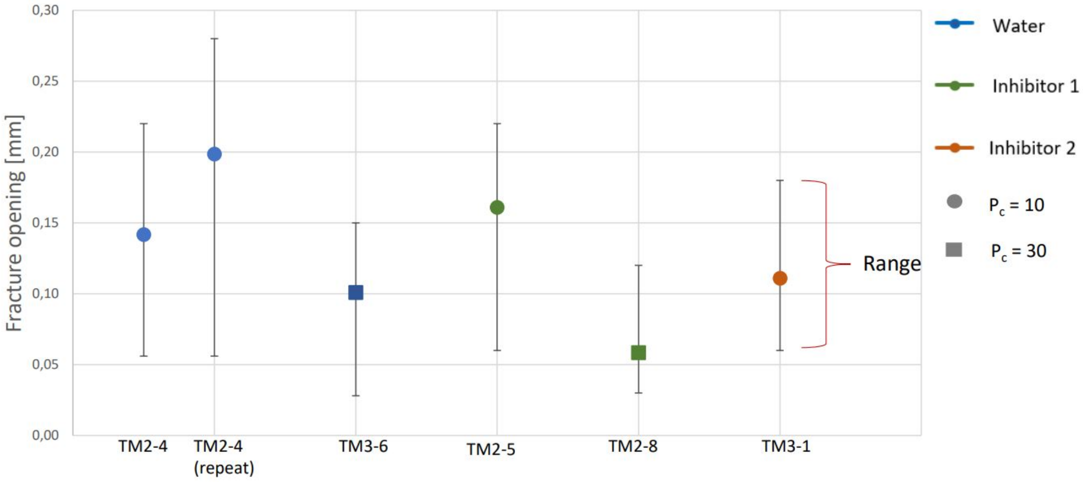

Figure 40: Aperture measurements were performed at regular intervals on equidistant horizontal slices. The results are graphically shown here. Note that the error bar shows the range of observations for each sample. The TM2-4 measurement was performed twice on separate a occasion to establish any potential interpretation error. A substantial error was found as shown graphically in this figure.

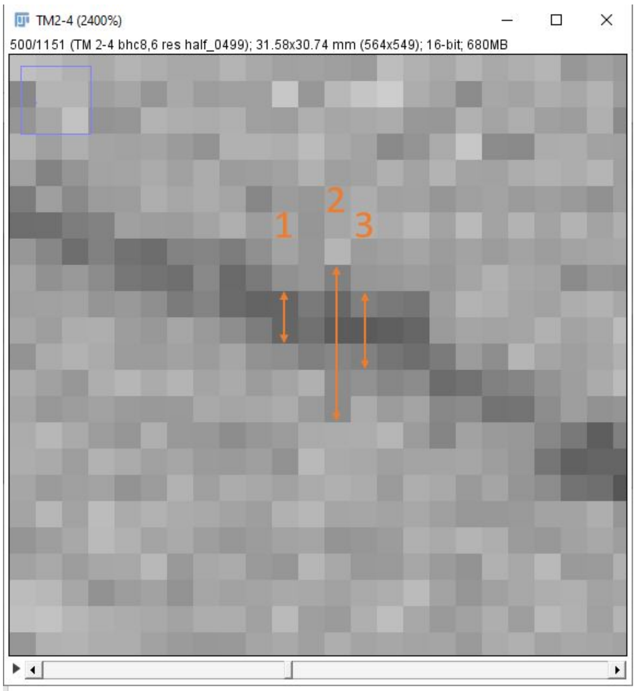
TM2-4 (2400%)

500/1151 (TM 2-4 bhc8,6 res half_0499); 31.58x30.74 mm (564x549); 16-bit; 680MB

Figure 41: The aperture measurement is strongly dependent on the location. Even adjacent voxels can already show a significant difference in apparent aperture, making the interpretation of the data difficult. The picture above illustrates how the fracture aperture measurement at three adjacent locations can yield completely different values: At 1 the aperture is measured as 0.11 mm, at location 2 and 3 this value is 0.31 and 0.18 mm respectively.

C Mohr-Coulomb variability

This section illustrates how the experimental variability was applied on the Mohr-Coulomb failure criterion. As discussed in section 3.5.2, some spread is expected when performing experimental tests on rock specimen. The effects of this spread are also present in the subsequent interpretation of the resulting data. The following example shows how this thesis accounts for this effect using an example with two experiments called experiment A and experiment B. Where experiment A was performed at a low P_c and experiment B was performed at a high P_c. Resulting in σ_{1A}, σ_{3A}, σ_{1B} and σ_{3B}. In this example repeat experiments on this rock type have shown that the rock strength has a range of R. Section 3.5 explains how these two experiments are used to generate a Mohr-Coulomb failure envelope. Figure 42 shows the base Mohr-Coulomb failure criterion. Then R is used to generate two additional sets of Mohr-Coulomb failure envelopes. The first set of half-circles results in an envelope with a lower value for S_0 and a higher value for μ. This set is generated by subtracting R from σ_{1A} and adding R to σ_{1B}, as shown in figure 43, such that:

$$\sigma'_{1A} = \sigma_{1A} - R \tag{18}$$

$$\sigma'_{1B} = \sigma_{1B} + R \tag{19}$$

With these new Mohr half-circles, the modified failure criterion is generated using the same method as explained in section 3.5. In a similar fashion, a Mohr-Coulomb failure envelope can be constructed with a higher value for S_0 and a lower value for μ. Therefore R should be added to σ_{1A} and subtracted from σ_{1B}. Such that:

$$\sigma''_{1A} = \sigma_{1A} + R \tag{20}$$

$$\sigma''_{1B} = \sigma_{1B} - R \tag{21}$$

The resulting Mohr-Coulomb failure criterion is shown in figure 44
The two resulting linear envelopes will give an estimated outer boundary of the experimental variability based on R.

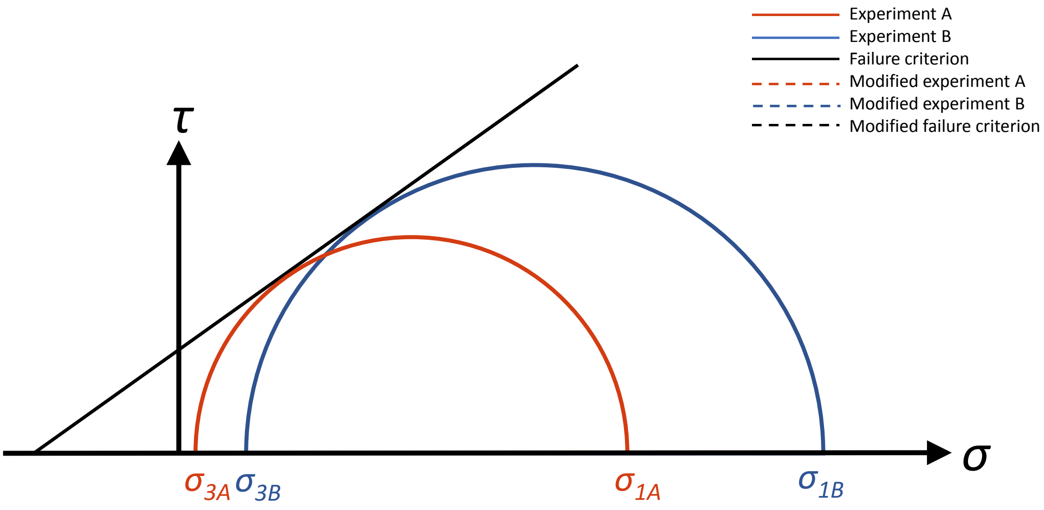

Figure 42: Original Mohr-Coulomb failure criterion.

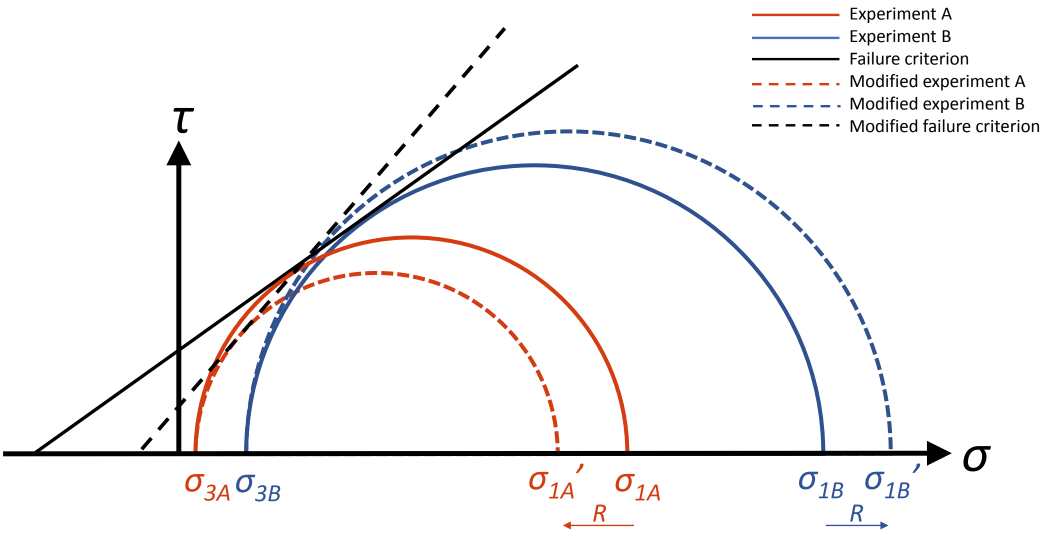

Figure 43: Original and modified Mohr-Coulomb failure criterion resulting in a criterion with a lower S_0 and a larger μ

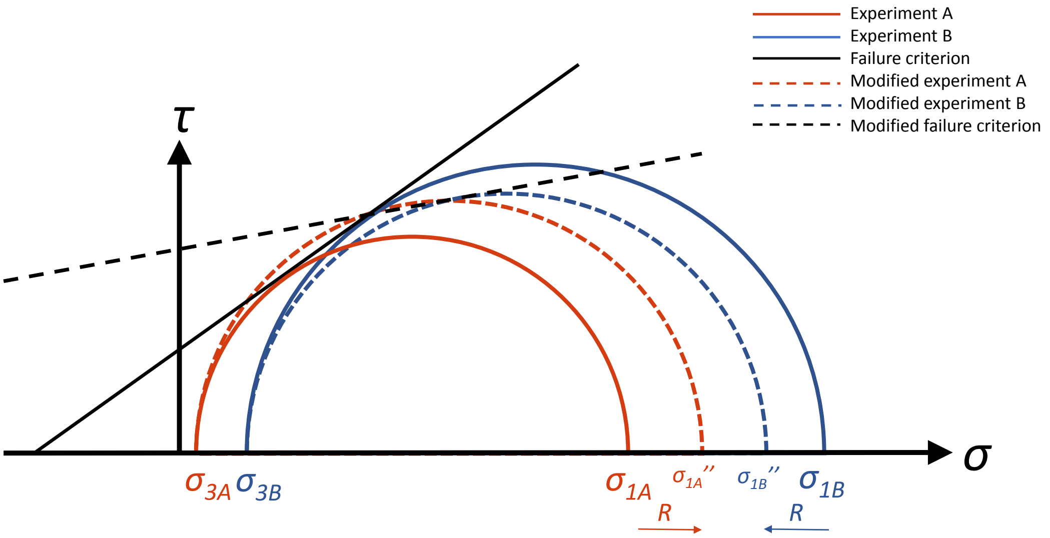

Figure 44: Original and modified Mohr-Coulomb failure criterion resulting in a criterion with a larger S_0 and a lower μ

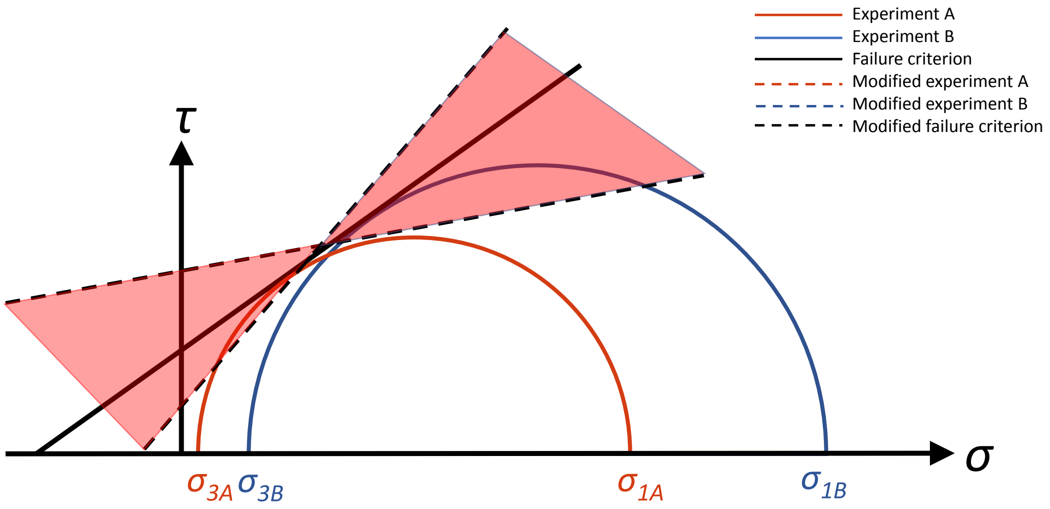

Figure 45: Combining both modified versions of the Mohr-Coulomb failure criteria gives an indication of the range of the Mohr-Coulomb failure criterion due to the experimental variability.

D Machine calibration

The triaxial experiment uses a set of LVDT's which measure the total displacement of the bottom loading piston. This displacement accounts for the sample rock deformation ϵ_s as well as deformation in the parts of the set-up that are affected by the axial loading. These parts include the end-caps and the platens used to mount the Hoek cell in place. In order to quantify this set-up (or machine) deformation ϵ_{md}, a number of calibration runs were performed. For these runs an aluminium cylinder was used instead of a rock sample. The cylinder had a length of: 60.03 mm, a diameter of 30.00 mm and a Young's Modulus of 69 GPa (e.g. ToolBox (2020)). During the axial loading, the total deformation (denoted as ϵ_t) is recorded. The elastic sample deformation as a function of axial load can be calculated using Hooke's Law as described in section 3.5. For the aluminium calibration sample this can be expressed as equation: 22. Here ϵ_{alu} indicates the strain in the aluminium sample, and the E_{alu} indicates the Young's Modulus for aluminium. The difference between the total deformation ϵ_t and the sample deformation ϵ_s must be due to the machine deformation ϵ_{md} (equation: 23). The machine deformation was then saved as a function of load. So that the triaxial tests performed on actual rock samples the machine deformation could be subtracted from the measured total deformation (equation: 24).

$$\epsilon_{alu} = \frac{\sigma}{E_{alu}} \tag{22}$$

$$\epsilon_{md} = \epsilon_t - \epsilon_{alu} \tag{23}$$

$$\epsilon_s = \epsilon_t - \epsilon_{md} \tag{24}$$